Dynamic tensile mechanisms and constitutive relationship in CrFeNi medium entropy alloys at room and cryogenic temperatures

Kai Wang, Xi Jin, Yong Zhang, Peter K. Liaw, and Junwei Qiao

Phys. Rev. Materials **5**, 113608 — Published 30 November 2021

DOI: 10.1103/PhysRevMaterials.5.113608

Dynamic tensile mechanisms and constitutive relationship in CrFeNi medium entropy alloys at room and cryogenic temperatures

Kai Wang[1], Xi Jin[1], Yong Zhang[2], Peter K. Liaw[3], Junwei Qiao[1,*]

1. *College of Materials Science and Engineering, Taiyuan University of Technology, Taiyuan 030024, China*
2. *State Key Laboratory for Advanced Metals and Materials, University of Science and Technology Beijing, Beijing 100083, China*
3. *Department of Materials Science and Engineering, The University of Tennessee, Knoxville, TN, USA*

Abstract

Harsh service conditions in the aerospace, defense and military, and other fields are calling for materials with excellent mechanical properties to undergo extreme deformation (such as elevated and cryogenic temperatures, and high strain rates) without sustaining damage while retaining high strength. Outstanding mechanical properties of high/medium entropy alloys (HEAs/MEAs) render them potential as candidates. In this study, as the temperature decreases, a breakthrough of the strength-ductility trade-off is achieved in a CrFeNi MEA with partially recrystallized face-centered-cubic (FCC) phases, together with body-centered-cubic (BCC) precipitates. At a strain rate of 3,000/s, the yield strength is increased from 920 MPa at 298 K to 1,320 MPa at 77K, while the uniform elongation increases by 28.5%. This phenomenon

* Corresponding author. E-mail: qiaojunwei@gmail.com

also occurs at quasi-static tension. Under low-temperature loading, nanotwins are popularly activated due to the decreased stacking fault energy (SFE) with decreasing temperatures. A positive strain-rate dependent yield strength arises, owing to the contributions from the short-range dislocation obstacles, BCC phases, and refined grains. High-density dislocations and BCC phases result in the degeneration of uniform elongation, specially with the increase of strain rates. Strain-rate-dependent and temperature-dependent constitutive models were successfully established to predict the deformation behaviors of CrFeNi MEAs under such a wide range of strain rates at room and cryogenic temperatures.

Keywords: Medium-entropy alloy; Mechanical property; High strain rates; Cryogenic temperature; Constitutive modeling

1. Introduction

Extreme conditions, such as elevated and low temperatures, high pressures, high deformation rates, strong radiation, etc., often exist in aerospace, defense and military, reactor, industrial and other fields. With the development of these advanced industries, more and more stringent requirements for high-performance structural materials are increasingly expected. In contrast, most traditional metals and alloys always face the strength-ductility trade-off dilemma especially under extreme conditions [1-3], and cannot meet these extreme requirements. High-entropy alloys (HEAs), also known as multi-principal element alloys or complex concentrated alloys, break through the strength-ductility trade-off, i.e., simultaneously strong and ductile [3-5]. Generally, HEAs process much more metastable states, compared with conventional dilute alloys, and thus, broader tailorable mechanical properties are available. In particular, under extreme conditions, outstanding resistances and large tolerances to external sufferings can be popularly realized in HEAs, such as outstanding elevated [6-8] and cryogenic [9-11] temperature performances, super welding properties [12], good fatigue [13, 14] and fracture resistance [4, 15] and good hydrogen embrittlement [16]. These excellent properties render them potential to be the next generation of structural materials.

Usually, HEAs/MEAs (medium-entropy alloys) with single face-centered-cubic (FCC) structures show excellent ductility but relatively low strengths [17, 18], while body-centered-cubic (BCC)-structured HEAs always display high strengths but relatively-poor ductility [18]. Gratefully, if dual-phase (FCC + BCC) HEAs are

properly designed, a good combination of strength and toughness may be achieved [19, 20]. Herein, a duplex FCC + BCC CrFeNi MEA subjected to proper thermomechanical processing was developed in this study.

During load-bearing services for structural materials, it is inevitable to suffer from high-speed loadings. To further promote the application of HEAs/MEAs under extreme loading, it is imperative to reveal their dynamic mechanical behavior and microscopic-deformation mechanisms. Up to now, the studies mainly focus on the dynamic compression of HEAs/MEAs [21-27]. However, the dynamic tensile behavior has been rarely investigated [3, 28, 29]. It should be mentioned that tension and compression asymmetry is generally present in almost all alloys[30, 31]. Meanwhile, these studies mainly focus on the dynamic deformation at room temperature, and the studies on the dynamic deformation at cryogenic temperature is lacking. Therefore, it is urgently necessary to explore the dynamic tensile behavior of HEAs/MEAs, specially at cryogenic temperatures.

In this study, the microstructural evolution and mechanical behavior of the CrFeNi MEA upon quasi-static and dynamic tensile loading (at strain rates of 2,000 - 4,000/s) at room temperature (298 K) and cryogenic temperatures (77 K) were investigated in detail. The deformation mechanisms of the present MEAs with high strengths and considerable elongations under low temperatures or/and high strain rates were explored. Meanwhile, quantitatively, the strain rate-dependent and temperature-dependent constitutive models are exactly established to predict the deformation behavior of CrFeNi MEAs over a wide range of strain rates at room and cryogenic

temperatures.

2. Experimental

The material used in the present study was an equiatomic MEA with a nominal composition of CrFeNi. The samples with dimensions of 80 mm × 22 mm × 2 mm were cast in a vacuum arc melting furnace with suitable copper-moulds, using high-purity constituent elements (purity>99.9% weight percent, wt.%). The ingots were flipped and remelted at least five times to ensure thorough mixing and chemical uniformity. As-cast plates were homogenized at 1,200 □ for 2 h to eliminate the dendrite segregation and obtain a single FCC structure with equiaxed grains about 160 μm, which has been displayed in the previous work [32]. Then, they were multi-pass cryo-rolled up to 70% reduction in thickness (final thickness of ~ 0.6 mm), using a laboratory-scale rolling mill. During the cryo-rolling, the specimens were immersed in liquid N_2 for 10 minutes before each pass. The cryo-rolled sheets were subsequently annealed at 800 □ for 1 h, followed by water quenching.

Rectangular dog-bone tensile specimens for quasi-static and dynamic tensile tests were machined with the tension axis oriented along the rolling direction, and they were carefully ground down to a 2,000-grit SiC paper. The gage dimensions (width, thickness, and length) of quasi-static and dynamic tensile specimens were 4 × 0.6 × 10 mm^3 and 4 × 0.6 × 5 mm^3, respectively. Quasi-static uniaxial tensile tests were conducted at a strain rate of 1×10^{-3} /s and temperatures of 298 K and 77 K, using an Instron 5969 testing machine. Dynamic tensile tests were carried out at strain rates of

3,000/s and temperatures of 298 K and 77 K, using a modified split Hopkinson tensile bar (SHTB) apparatus. Before cryogenic-temperature tests, the specimens were entirely immersed in a bath of liquid nitrogen for at least 10 minutes. During the entire cryogenic tension, liquid nitrogen was continuously added to ensure that the samples were completely immersed in a bath of liquid nitrogen. To investigate the strain-rate sensitivity, tensile properties at strain rates of 1×10^{-4}, 1×10^{-1}, 2,000, and 4,000/s were investigated at 298 K. All the tests were repeated at least three times at each strain rate and temperature to confirm reproductivity.

Phase structures of samples before and after tension were recognized by X-ray diffraction measurements on a Rigaku Ultimata IV X-ray equipment, using Cu Kα radiation. The scanning rate of 4°/s and the range of 20° - 100° were applied. The microstructures were examined, using scanning electron microscopy (SEM) equipped with an electron backscatter diffraction (EBSD) on JEOL JSM-7100F field emission gun-scanning electron microscopy. The accelerated voltage of 25 kV and scanning step size of 0.3 μm are chosen to obtain EBSD data. The EBSD samples were polished with 2,000-grit SiC paper and subsequently electrochemically polished, using a 10% perchloric acid + 90% ethyl alcohol (volume percent) at a direct voltage of 15 V at room temperature. Transmission electron microscopy (TEM) investigations were conducted on a JEOL-2100 TEM operated at 200 kV to examine detailed structures before and after tension to reveal strain-rate-dependent and temperature-dependent deformation mechanisms. The TEM samples were first mechanically ground to a thickness of 50 μm and then twin-jet electropolished using 10% perchloric acid + 90% ethyl alcohol

(volume percent) at - 25 □, followed by Ar-ion milling to suitable thickness.

3. Results

3.1 Microstructures

X-ray diffraction (XRD) patterns of as-cast and as-annealed samples are shown in Fig.1a. As expected, a set of BCC diffraction peaks are found after annealing at 800□ for 1 hour. The lattice constants of both FCC and BCC phases were estimated to be 0.3597 and 0.2886 nm, respectively. Figure 1b presents the bright-field (BF) TEM image and corresponding select-area electron diffraction (SAED) patterns of the sample before deformation. The SAED patterns further confirm an FCC + BCC duplex structure. In addition, energy diffraction spectrum (EDS) point analyses were performed on the two grains indicated by the yellow arrows in Fig. 1(b), and the results are summarized in Table 1. It is noted that the BCC phase is mainly enriched in Cr, while the FCC phase has an almost equal content of three elements. The volume fraction of FCC and BCC phases were counted to be ~ 90% and ~ 10 %, respectively, based on the XRD pattern and numerous BSE maps. The Cr-rich BCC phases are also found in other Cr-containing HEAs [33-35] and stainless steels [36].

Several factors account for the availability of Cr-rich precipitates. Firstly, from the view of the average valence electron concentration (VEC), which is a well-developed parameter to predict the solid-solution phase formation in multi-principal elements alloys, the value of VEC is 8 for current CrFeNi MEAs. As is known to all, VEC values of 8 and 6.8 are the critical values to distinguish the single FCC region and

single BCC region, respectively. [37]. Some HEAs or MEAs with VEC of 8, such as $Al_{0.8}$CoCrCuFeNi [38] and AlCuNi [38], have an FCC + BCC duplex structure. Secondly, Cr is a BCC-phase stabilizer [37]. Based on calculations from the CompuTherm software (shown in Figure S1[39]), for $Cr_x(FeNi)_{100-x}$ alloy systems, the maximum Cr content for a single FCC phase structure at 800□ is 28.6% (atomic percent, at. %). At relatively-low temperatures, the solid solubility of atoms, especially the Cr atom with a higher melting point, is significantly reduced in the matrix, which easily causes the formation of Cr-rich secondary precipitates. Besides, Cr has a higher diffusion coefficient, compared with Fe and Ni atoms, which may facilitate its precipitation from the matrix [40]. And thirdly, partial pair correlation functions ($g_{\alpha\beta}$), which is a key parameter to predict the existence of elemental preferential short-range ordering (SRO), can be used to investigate SRO in current CrFeNi MEAs [41]. The $g_{\alpha\beta}$ values from *ab* initio molecular dynamics (AIMD) simulations show that certain nearest-neighbor pairs, such as Cr-Cr and Cr-Fe, occur much more frequently than others (for example, Ni-Ni, Ni-Fe, and Ni-Cr) [41]. These SRO can be regarded as precursors for nucleating segregated Cr-rich phases[41]. As a consequence, Cr-rich precipitates are available in the present MEA.

Meanwhile, some areas with high dislocation densities are found in Fig. 1b, which are considered as non-recrystallized zones. The heterogeneous structure was demonstrated by an inverse pole figure (IPF) of EBSD, as shown in Fig. 1c. Both partially-recrystallized regions with fine grains and coarsened non-recrystallized grains co-exist. Analogous combinations of such heterogenous structures have come about in

CrCoNi MEAs [42]. The volume fraction of the recrystallized region was estimated to be ~ 42% from IPF images. An average grain size of the recrystallized FCC phase is 760 nm, and that of the BCC phase is 355 nm. Moreover, the corresponding local misorientations were observed in the EBSD kernel average misorientation (KAM) map, as presented in Fig. 1d. It indicates that the dislocation density in the non-recrystallized regions is higher than that in the recrystallized ones.

3.2 Mechanical properties

Figure 2a exhibits the representative quasi-static and dynamic tensile engineering stress-strain curves tested at room and cryogenic temperatures, and the tensile properties are summarized in Table 2. For convenience, the specimens deformed under quasi-static (10^{-3}/s, Q) and dynamic (3,000/s, D) at room temperature (298K) and cryogenic temperature (77K) are referred to as 'Q298', 'Q77', 'D298', and 'D77', respectively. The dimples are popular on all the rupture surfaces, typical of ductile fracture (shown in Figure S2[39]). The average yield tensile strength (YS), average ultimate tensile strength (UTS), and average uniform elongation (UE) of Q298 are 605 ±6 MPa, 785±12 MPa, and 18±1%, respectively. At a constant strain rate of 10^{-3}/s, as the decreases of temperature from 298K to 77K, both the strength and ductility increase. The average YS and UTS are increased to 940 MPa and 1,220 MPa, respectively. Meanwhile, the UE of Q77 is 29%. This notably simultaneous improvement of strength and elongation is commonly achieved in FCC-based HEAs [5, 43]. Astonishingly, the strength and ductility of D77 are increased simultaneously, as compared with D298. The YS, UTS, and UE of D77 reach 1,320 ± 12 MPa, 1,530 ± 15

MPa, and 9 ± 1%, respectively. In brief, under a constant strain rate, the lower the tested temperature, the stronger and tougher for the current MEAs, in consistency with previous studies [4].

Figure 2(b) displays the true stress-strain curves of Q298 and Q77 specimens and the corresponding work-hardening rate (WHR) curve. Since the work-hardening fluctuation is severe under dynamic loading, it is not considered in the present work. Obviously, the WHR of the Q77 specimen is much higher than that of the Q298 one, and it is possible that there are extra strengthening mechanisms associated with the increased lattice-friction resistance at 77K. The onset of localized deformation (plastic instability or necking) during tension could be determined by a Considére criterion, as expressed as $\frac{d\sigma}{d\varepsilon} \leq \sigma$ (Here, σ and ε are true stress and true strain, respectively) [44]. The intersections of the WHR and true stress is plotted in Figure 2(b). The true strain at the beginning of necking in Q298 is 0.17, while that of the Q77 is 0.24. At 77 K, the improvement of the work-hardening ability can essentially delay necking, and hence, the fracture strain is accordingly enhanced. Moreover, the enhanced work-hardening capability facilitates the increase of the UTS. The UTS of the Q77 specimen is 1,575 MPa, while it is only 945 MPa in the Q298 specimen.

To illustrate the simultaneous improvement of strength and ductility in the current CrFeNi MEA, the correlations between the percentage change of YS and UE with deformation temperatures decreased from 298K to 77K at constant strain rates of 10^{-3}/s or 3,000/s are displayed in Figure 3. In comparison, much more data are collected from many kinds of metals and alloys, including pure elements, stainless steels, dual-

phase steels, twinning-induced plasticity (TWIP) steels, transformation-induced plasticity (TRIP) steels, titanium alloys, magnesium alloys, metallic glass matrix composites, and HEAs[26, 31, 45-57]. Detailed data are listed in Table S1[39]. Relative to other alloys, the CrFeNi MEA exhibits a higher value of the product of the change percentage of YS and the change percentage of UE. Generally, the temperature sensitivity of YS is increased as the solute concentration increases, which has been confirmed by Wu et. al. [17]. The highest solute concentration results in a current ternary equiatomic MEA. And, the pure BCC metals usually display greater temperature sensitivity of YS than pure FCC metals [17, 48]. There are 10% (volume percent) BCC phases in the CrFeNi MEA, and consequently the temperature sensitivity is higher than those alloys, such as $V_{10}Cr_{10}Fe_{45}Co_{35}$ with single FCC phases. Besides, the low stacking fault energy (SFE) of the FCC matrix, calculated based on large-scale atomistic simulations, promotes the dynamic formation of deformation twins, which substantially increases the strain-hardening ability, leading to the superior tensile ductility at cryogenic temperatures [58, 59].

Figure 4 shows the engineering stress-strain curves at different strain rates upon room-temperature tension, and the correspondingly-measured tensile properties are summarized in Table 2. The YS is almost doubled, from 550 to 1,010 MPa, with an increase of the strain rate from 1×10^{-4} to 4,000 /s, and it may be attributed to a typical strain-rate hardening effect [60, 61]. But UE is decreased from 21 to 4 %, accordingly. The higher the strain rate, the stronger but the less ductility for most metals and alloys. Strain-rate sensitivity (SRS), m, is often employed to characterize the strain-rate effect,

which is defined by the slope of the logarithmic flow stress versus the logarithmic strain rate. The inset presents the SRS of CrFeNi MEAs, which can be classified into two distinct regions: Regions I and II. Accordingly, the strain-rate sensitivity of the two regions, m_s (quasi-static) and m_d (dynamic), are calculated to be 0.0371 and 0.33968, respectively. Apparently, the strain-rate strengthening is more significant upon dynamic tension, which is common in FCC-based HEAs [3, 62].

4. Discussion

4.1 Deformation mechanisms

4.1.1 *Dislocations*

Figure 5 displays the EBSD Kernel Average Misorientation (KAM) maps of FCC phases in Q298, Q77, D298, and D77. Corresponding average KAM values and the density of geometrically necessary dislocations (GNDs) are summarized and displayed in Figures 5 (e-f), respectively. The average KAM values of Q298, Q77, D298, and D77 are calculated to be 0.786, 1.68, 0.763, and 0.455. The density of GNDs can be estimated, using the relationship of the density of GNDs, ρ^{GND}, and misorientation angle, θ, (i.e., the KAM value), and it is expressed as follows [63]:

$$\rho^{GND} = 2\theta/\mu b \quad (1)$$

where b is the magnitude of the Burgers vector ($b = \frac{\sqrt{2}}{2} \times a =$ 0.254 nm), a is the lattice constants of FCC phases calculated from XRD patterns. μ is the unit length ($\mu = 10^{-5}\ m$) [63]. The densities of GNDs in Q298, Q77, D298, and D77 are estimated to be $6.14 \times 10^{14}/m^2$, $1.32 \times 10^{15}/m^2$, $6.01 \times 10^{14}/m^2$, and $3.58 \times 10^{14}/m^2$,

respectively. Obviously, the fractured Q77 samples have the highest density of GNDs, which gives a clue that the contribution of GNDs to the work hardening of Q77 is the largest. It agrees with that the value of $\sigma_{uti} - \sigma_y$ is the greatest in Q77.

The TEM analyses of dislocation structures in Q298, Q77, D298, and D77 are presented in Figure 6. Tangles of randomly-distributed dislocations are found from the matrix of four samples, and no dislocation cell appears. There are a large amount of dislocations piling up at the boundaries of FCC and BCC phases. Slip lines can be found to intersect in Cr-rich BCC precipitates, especially in samples deformed plastically at 77K. Slip-slip interactions (forest hardening) can further contribute to growing stress levels with straining [64]. Similar slipping is uncovered in FCC + BCC duplex alloys, including $Al_{0.6}CoCrFeNi$ [62] and $Al_{0.5}FeCoCrNi$ HEAs [64].

4.1.2 *Structure transformation*

In addition, for Cr-rich alloys, such as 18Cr8Ni stainless steels, martensite transformation easily takes place upon heavily-plastic deformation [65]. But from the XRD patterns of Q298, Q77, D298, and D77 shown in Figure S3[39], similar phase transformation is absent during the whole tension, which may be attributed to that the weight fraction of Ni is much higher than that in the traditional austenitic stainless steel, while Ni is a austenite stabilizer [66]. Besides, Zhao et al. [67] and Ming et al. [68] found the presence of amorphous bands in deformed CrMnFeCoNi and $Cr_{26}Mn_{20}Fe_{20}Co_{20}Ni_{14}$ HEAs. In this study, numerous of TEM analysis rules out amorphous phases induced by shear banding. Significant dislocation accumulation in a constrained region inside shear bands, which raise the free energy of the original FCC

phase to a point higher than that of amorphous phases. Then the energy difference drives transformation [68]. The critical dislocation density for the transformation is proportional to the SFE [67]. The SFE of the current MEA is calculated to be 65.85 mJ/m^2 (298K) and 43.30 mJ/m^2 (77K) (the detailed calculation can be found in supplementary materials[39, 59, 69-78]), which is more than several times of that of $Cr_{26}Mn_{20}Fe_{20}Co_{20}Ni_{14}$ HEAs [68]. In other word, the critical dislocation density for phase transformation in the current CrFeNi MEA is about several times than that of the $Cr_{26}Mn_{20}Fe_{20}Co_{20}Ni_{14}$ HEA. Thus, amorphization is absent in the current CrFeNi MEA.

4.1.3 *Twinning*

Figure 7 shows the EBSD band contrast maps with Σ3 twin boundaries, which were marked in yellow. Surprisingly, twin boundaries popularly exist in all four samples. Owing to the limit resolution of EBSD, and the thickness of deformation twins being as small as a few nanometers, individual twins cannot be powerfully captured by EBSD technique. In other words, the twin boundaries observed in the band-contrast maps may be deformation-twin bundles (DTBs) [3]. The areal fraction of the DTBs in the fracture samples are estimated to be 2.2%, 7.4%, 4.2% and 6.1% using the corresponding relative frequency of misorientation angles, respectively. Alternatively, the TEM technique with a better spatial resolution was adopted to identify individual twins, as presented in Figure 8. There are no parallel bands available in Q298, and thus, the twin boundaries from EBSD band-contrast maps can be caused by special grain orientation, as happens in TWIP steels [79]. Thus, the deformation twins play nearly zero effects on the work-hardening rates during quasi-static deformation at 298K. In

contrast, profuse parallel bands are found in Q77, D298, and D77. Both high-resolution TEM maps and selected area electron diffraction (SAED) map (almost the same for three conditions) uncover that these parallel bands are deformation twin bundles (DTBs). The average twin thicknesses are estimated to be 2.5 nm, 11.6 nm, and 5.3 nm for D298, Q77, and D77, respectively, based on numerous high-resolution TEM maps. The areal fractions of the matrix and twin lamellae in the DTBs are almost the same, both of which are ~ 50%. Combining the results from EBSD and TEM observations, the twin fractions in D298, Q77, and D77 are finally evaluated to be 2.1%, 3.7%, and 3.1%, respectively.

It is well established that either a decrease in temperatures or an increase in strain rates could facilitate twinning relative to slipping due to restricted dislocations [80-82]. For instance, in $V_{10}Cr_{15}Mn_5Fe_{35}Co_{10}Ni_{25}$ HEAs, a slip-TWIP transition with decreasing temperatures was discovered [83]. Laplanche et al. [84] proposed that twins could be generated during successively plastic straining at room temperature, when the stress was larger than the critical stress for twinning. Thus, the critical stress required for twinning governs the initial twinning. It has been demonstrated that the predicted values of the critical twinning stress for CoCrFeNi HEAs could be well calculated, using the Steinmetz equation [71]. According to Steinmetz et al. [85], the critical stress required for twinning is expressed as:

$$\sigma_T = \frac{M\gamma_{SFE}}{3b_p} + \frac{3Gb_pM}{L_0} \quad (2)$$

where σ_T is the critical stress for twinning, γ_{SFE} is the SFE, M is the Taylor factor (taken as 3.06), and b_p is the Burgers vector of the partial dislocations with $b_p =$

$0.254\ nm$ [86]. The values of SFE at 298 K and 77 K are substituted into *Eq. (2)*, and the critical stresses required for twinning are obtained. The critical twinning stress for the FCC phase of CrFeNi MEAs at 298 K is 1,069 MPa, while the UTS of Q298 and D298 are 932 MPa and 1,178 MPa, respectively. In other words, upon tensile straining at 3,000/s, and the twinning takes place at a true plastic strain of 3.55%.

Generally, the higher of the strain rate, the larger velocity for dislocation movement. Hence, dislocation pile-ups easily come about and further result in localized stress concentration that acts as effective nucleation sites for deformation twins. Woo et al. [87] have found that a large amount of stacking faults/twins in CoCrNi MEAs at high strain rates, which increase the stacking fault probability (SFP) and in turn, drives the decrease of the SFE. The critical twinning stress for the FCC phase at 77K is 978 MPa, and the UTS of Q77 and D77 are 1,573 MPa and 1,666 MPa, respectively. Meanwhile, the YS of Q77 and D77 are 940 MPa and 1,320 MPa, respectively. As a consequence, the twinning occurs at a true plastic strain of 0.7% for Q77. But for D77, the true stress reaches the critical twinning stress at the beginning of plastic deformation. The theoretical calculations agree well with above observations that twinning is lacking in Q298, while deformation twins are widely found in Q77, D298, and D77. Therefore, at 77 K, the plasticity of FCC phases is partly originated from deformation twins. Dislocation slip can even occur in BCC phases to coordinate further straining caused by deformation twins generated in the FCC phases. It is concluded that the generation of deformation twins may promote the work-hardening capability [88]. Nanoscale twin boundaries could act as effective barriers against dislocation movement and reduce the

mean free path of dislocation glide like grain boundaries, known as the dynamic Hall-Petch effect. The activation of profuse twin systems at 77 K leads to a significant improvement of the work-hardening capacity for the current CrFeNi MEA. Furthermore, according to the Considére criterion [44], twin-induced hardening can delay plasticity instability to a higher strain. Therefore, CrFeNi MEAs have higher tensile strengths and larger elongations at 77 K than that at 298K.

4.1.4 *Excellent mechanical properties upon dynamic loadings*

For CrFeNi MEAs, the yield strengths were significantly increased upon dynamic loading, since the dislocation motion becomes popular under high strain-rate loading [3, 26]. The fracture strain decreases upon dynamic tension, since the stress concentration may happen from the heterogeneous distribution of dislocations, originating from insufficient recovery upon low-temperature annealing. Similar results have been revealed in the pre-strained AISI 301LN2B metastable austenitic stainless stees [89]. The uniform elongation of this kind of steels with high-density dislocations is decreased as the strain rate increases, while samples with few dislocations show an opposite trend.

Apart from the heterogeneous dislocation structure, the complex microstructure may affect the strain-rate-dependent plasticity. For instance, for single-phase $V_{10}Cr_{10}Fe_{45}Co_{30}Ni_5$ [90] and CoCrFeNi [91] FCC HEAs, the strength is significantly enhanced, and meanwhile, the uniform elongation remains almost unchanged upon dynamic loading, since successive twinning is accompanied. For conventional BCC metals and alloys, a positive strain-rate effect exists in the yield

strength, but the negative one occurs in plasticity [92]. In comparison, the HEAs with an FCC + BCC + B2 structure [22, 28] from dynamic compression display a strength-ductility trade-off. Compared with the quasi-static compression, the strength of HEAs with a BCC1 + BCC2 structure [24] upon dynamic compression is improved, and the uniform elongation is reduced. These results verify analogous strain-rate-dependent strength or plasticity in HEAs/MEAs, as found in traditional BCC metals and alloys.

To sum up, the twinning in the FCC phases usually leads to an increased uniform elongation, but the BCC phases usually decrease it. Therefore, high-density dislocations, together with BCC phases within the FCC matrix, reduce uniform elongations in D298 and D77.

Based on the above analysis, the microstructure evolution subjected to the thermomechanical treatment and plastic straining for the current CrFeNi MEAs are schematically depicted in Fig. 9. The initial microstructure after homogenization is composed of coarse FCC grains with few dislocations. After rolling and annealing, the heterogeneous structure appears, which consists of the coarse uncrystallized grains, recrystallized dislocation-free FCC grains, and recrystallized dislocation-free BCC grains. Before loading, the dislocations are mainly concentrated in the coarse uncrystallized grains, and twinning is not activated. Subjected to quasi-static tension at 298 K, dislocations are generated within the recrystallized FCC grains. It indicates that slipping prevails during quasi-static and room-temperature tension. After dynamic tension at 298 K, due to strong and positive strain-rate sensitivity, the strength of D298 is much higher than that of Q298, and it is easy to reach the critical twinning stress.

Twinning takes place in the recrystallized FCC grains. Upon tension at 77 K, a lower SFE results at cryogenic temperatures, which can promote continuous twinning (nucleating at initial dislocation pile ups). Twinning prevails within the recrystallized FCC grains even at low strains (＜1%). Meanwhile, dislocations dominate within the recrystallized BCC grains upon heavily-plastic deformation. Since brittle BCC phases may result in stress concentration, the uniform elongation is lower at high strain rates. As a result, a premier failure happens for D77. Both the volume fraction of twins and dislocation density of Q77 are higher than those of D77, as there is insufficient time for dislocations or twins to develop.

4.2 Strain-rate sensitivity

The value of quasi-static SRS (m_s) as well as dynamic SRS (m_d) of some HEAs/MEAs together with many metals and alloys under tension are listed in Figure 10 and Table S2[3, 21, 25, 28, 29, 39, 46, 48, 49, 51, 52, 62, 82, 93-100]. Meanwhile, some quasi-static and dynamic SRS of HEAs and MEAs under compression are also included in Figure 10. Obviously, the m_s and m_d of HEAs, MEAs, and steels are remarkably higher than those of pure FCC metals and dilute FCC alloys, which may originate from strong short-range dislocation obstacles [3]. For HEAs and MEAs, the dislocation obstacles are popular, since strong Peierls-Nabarro barriers (i.e., lattice friction resistance) are available, including severe lattice distortions [101-103] and nanoscale inhomogeneities, including co-clusters and /or short-range chemical orders [104, 105].

From Figure 10, the present CrFeNi MEA has higher m than most HEAs and MEAs, which may be attributed to the ultra-fine grains of recrystallized microstructures and BCC phases, both of which have been proved to significantly increase SRS. For example, Komarasamy et al. [106] found that the strain-rate sensitivity reduced as the

grain size increased. The BCC-structured Nb [48] and Ta[49] display higher *m* than FCC metals under quasi-static loading. According to these studies, it is reasonable to infer a high *m* for the current MEA. However, compared with 316L stainless steels , the m_d of current CrFeNi MEA is lower [96]. m_d of 316L stainless steels are obtained from dynamic compression at 2,700/s, 4,200/s, 5,600/s, 6,900/s, and 7,500/s [96], while currently-investigated strain rates are of 2,000/s - 4,000/s, much lower than those for 316L stainless steels. As demonstrated above, more rapidly enhancement for the yield strength, i.e., high m_d, may arise upon high-speed loading due to the dislocation drag. Besides, tension-compression asymmetry exists frequently in most alloys[30, 31]. Previous studies have revealed that the value of *m* from compression is higher than that from tension [107, 108]. As a result, a lower m_d of the current CrFeNi MEAs come into being, compared with 316L stainless steels.

Furthermore, for metallic glasses (amorphous alloys) with disordered structures, since the high strain rate would dramatically increase adiabatic heating within shear layers, and the thermal softening plays a leading role, the yield strength was negatively correlated with the strain rate [109]. In contrast, by introducing crystalline phases, metallic glass matrix composites show a positive strain-rate sensitivity when the dislocation-strengthening mechanism is dominant. Hence, a moderate positive strain-rate sensitivity is achieved in such kinds of composites [110].

4.3 Constitutive relationship

4.3.1 *Strain-rate-dependent yield strength*

According to different dislocation velocities, mechanisms governing plastic

deformation can be divided into thermally-activated dislocation motion, dislocation drag, and relativistic effects mechanisms [111]. Thermally-activated dislocation motion mechanisms usually govern plastic deformation at low strain rates. For a pure FCC Cu, the dislocation drag should be considered only if the strain rate is larger than 24,000/s [112]. Recent investigations on the constitutive relation of CoCrFeNi HEAs upon dynamic tension ($\dot{\varepsilon} \geq 3000/s$) has been done [3]. A modified Zerilli-Armstrong (Z-A) model, which is a physically-based constitutive relationship, based on a thermally-activated dislocation motion theory, is well established by introducing the dislocation drag [3]. It is necessary here to testify the improved model in current duplex MEAs. A Z-A model is expressed as [113]

$$\sigma_y = \beta_0 \varepsilon^{1/2} \exp(-\beta_1 T + \beta_2 T ln\dot{\varepsilon}) + \sigma_G \quad (3)$$

where β_0, β_1, and β_2 are material constants, ε is the yield strain, and it takes values of 0.002, and T is the absolute temperature, and it is considered to be 298 K for room-temperature tension. σ_G is the athermal stress and taken as the grain-boundary strengthening for the current CrFeNi MEA. Here, we approximately adopted the value of a strengthening coefficient, k_y, from CoCrNi alloys, and it is 265 MPa $\mu m^{1/2}$ [44]. As is listed above, the average grain size of FCC phases in recrystallized zones (volume fraction of ~60%) is ~ 760 nm. Accordingly, the value, σ_G, is calculated to be 182.4 MPa. The experimental results from different strain rates are used to determine the parameters in *Eq. (3)*, and the values of β_0, β_1, and β_2 from best fitting are 4.85×10^5 MPa, 1.92×10^{-3}/K, and 1.23×10^{-4}/K, respectively. The strain-rate effects of σ_y in CrFeNi MEAs under quasi-static loading can be well described via *Eq. (3)* [see

Figure 11(a)]. However, an obvious deviation between the experimental results and theoretical predictions (black thread) comes about at a strain rate of 4,000 /s, indicating that there is an extra mechanism. It is reasonable to introduce the dislocation viscous drag into the traditional Z-A model, and it is employed as follows [112]:

$$\sigma_y = \frac{\beta_0 \varepsilon^{1/2} \exp(-\beta_1 T + \beta_2 T ln\dot{\varepsilon})}{(1-c\dot{\varepsilon})^{\beta_2 T}} + \sigma_0 \quad (4)$$

where c is a material parameter. The thermal-activation equation with dislocation drag [red thread in Figure 11(a)] could better capture the strain-rate effect of σ_y upon high-speed loading in the current MEAs, and *c* is determined to be 2.31×10^{-4} s.

Similarly, the yield strengths of Q77 and D77 are approximately predicted, using *Eq. (4)*, and they are 965 MPa and 1,103 MPa, respectively. The predicted results have 2.6% and 16.4% deviations from experimental values, respectively. On one hand, during the cryogenic tension, an extra deformation mechanism, twinning, prevails before yielding, and thus, it may have a positive effect on the enhancement of yield strength. On the other hand, the temperature-dependent yield strengths may be ignored due to the fact that the data for fitting from room-temperature tension. Consequently, the mismatch between the experiment results and theoretical predictions emerges. Further work is needed to exactly predict the yield strengths from different temperatures, and it will be our future work.

4.3.2 Strain-rate-dependent strain hardening

Upon dynamic loading for materials, three mechanisms are substantially popular: work hardening, strain-rate hardening, and thermal softening [111]. The first two generally trigger the increase of the isothermal flow stress, while thermal softening

always decreases it. Upon plastic straining, the plastic energy is usually converted into the heat, and it may trigger thermal softening [114]. The average temperature rise can be calculated by the following equation:

$$\Delta T = T - T_0 = \int_{T_0}^{T} dT = \frac{\beta}{\rho C_p} \int_0^{\varepsilon_p} \sigma d\varepsilon_p \quad (5)$$

where ΔT is the temperature rise, T is the instantaneous temperature, T_0 is the initial temperature, and it is considered as 298 K, ρ is the mass density, which is calculated to be 7.98 g/cm^3, C_p is the heat capacity, which is estimated to be 0.446 J/g K, according to the rule of mixture [115]. β is the fraction of the plastic energy converted to heat and chosen as 0.9 [53], and ε_p is the true plastic strain. Calculated by *Eq. (5)*, the temperature rises of 26.3 K, 23.5 K, and 15.3 K are obtained at the strain rates of 2,000, 3,000, and 4,000 s^{-1}, respectively, as shown in Figure 12(a). Hence, thermal softening is reasonably ruled out upon high-speeding loading.

In this study, a look at the microstructure evolution indicates that both dislocation strengthening and twinning strengthening contribute to work hardening. Based on the Taylor's hardening model, a microstructure-based constitutive model would be developed. The stress induced by forest dislocations can be described by [116]:

$$\sigma_f = M\alpha Gb\sqrt{\rho} \quad (6)$$

where M is the average Taylor factor, G is the shear modulus (taken as 69 GPa for current MEAs at 298 K [32]), α is a constant related to the dislocation interaction strength, and it is taken as 0.4 at 298 K [3]), ρ is the total dislocation density, which is estimated to be $1.592 \times 10^{13}\ m^{-2}$ (the detailed calculation can be found in supplementary material[39, 117]), and b is the Burgers vector for the perfect dislocation,

which is taken as 0.254 nm [32]. The evolution of the total dislocation density considering the competition between the dislocation storage and recovery can be calculated as follows [118]

$$\frac{d\rho}{d\varepsilon_p} = M(\frac{1}{b\Lambda} - k\rho) \quad (7)$$

where Λ is the mean free path, and the corresponding calculations are described below. k is the dynamic recovery factor depending on the strain rate and temperature, which can be written as follows [119]:

$$k = k_0(\frac{\dot{\varepsilon}}{\dot{\varepsilon}_0})^{-\frac{KT}{A}} \quad (8)$$

Here, k_0 is a recovery factor at 0 K, and K is Boltzmann constant, which is 1.38×10^{-23} J/K. $\dot{\varepsilon}_0$ is the reference strain rate, and it is taken as 10^7 /s [119]. T is the transient temperature during deformation, which is ignored since the calculated temperature rise is very small. A is a material parameter depending on the SFE (γ_{SFE}), and it can be calculated, based on a phenomenological equation [120]:

$$\frac{A}{Gb^3} = \frac{1}{\exp(1.44+27.55\xi-390.54\xi^2)} \quad (9)$$

where ξ is the normalized stacking fault energy ($\xi = \gamma_{SFE}/Gb$). Substituting the value of SFE, A is determined to be 2.4×10^{-19} J for the current MEAs at 298 K.

Based on above microstructural observations (the twinning plays a vital role upon dynamic tension while innocuous one upon quasi-static one), the only kind of impenetrable obstacles to dislocations motion are those related to the dislocation structure itself for the current MEAs under the quasi-static tension. As a result, $1/\Lambda$ is proportional to $1/\sqrt{\rho}$ for the current alloys under quasi-static deformation, regardless of the dislocation operations--completely random or a cell or subgrain structure [60],

i.e., $\Lambda = k_1\sqrt{\rho}$. In contrast, the nanotwin boundaries must be considered upon high-speed tension, i.e., $\Lambda = k_2\sqrt{\rho} + \frac{i_\Delta}{\Delta}$, with k_1 and k_2 being the relevant dislocation storage rates under quasi-static and dynamic conditions, respectively. i_Δ is a constant for scaling the contribution of the average twin spacing to the effective boundary distance, which is taken as 0.14 for current alloys with references to TWIP steels [120]. Δ is the average twin spacing, which can be established from the stereological analysis by Fullman [121]

$$\Delta = 2t\frac{1-F}{F} \tag{10}$$

where t is the average twin thickness, and F is the twin volume fraction, and its evolution can be captured, based on Olson and Cohen's equation [72]:

$$F = 1 - exp(-\varphi(\varepsilon_p - \varepsilon_{int})) \tag{11}$$

where φ is a strain-independent constant, and ε_{int} is a twinning initial strain determined by the critical twinning stress (σ_{crit}). It is expected that φ is dependent on the SFE and strain rates, with an increase resulting from decreasing fault energies and/or increasing strain rates, since these factors tend to favor twinning rather than dislocation slip [72]. The critical stress required for twinning is estimated to be 1,069 MPa upon room-temperature quasi-static deformation. And, the initial twinning strains take values of 7.4%, 3.55%, and 1.5% at strain rates of 2,000/s, 3,000/s, and 4,000/s, respectively. Combining the ε_{int} and the twin fraction experimentally obtained above, φ is calculated to be 0.653 at 298 K.

Therefore, the above equations *Eqs. (6)-(11)* fully describes the current constitutive relation of CrFeNi MEAs under quasi-static and dynamic tension at room

temperature. All the material constants and parameters used in the model are listed in Table 3. k_1, k_2, and k_0 are the parameters, which are needed to be determined by fitting stress-strain curves. The fitting parameters from best fits are also summarized in Table 3, and the corresponding model prediction and tested results are depicted in Figure 12b. The plastic flows at different strain rates are almost exactly predicted, using the parameters obtained by fitting, as shown in Figure 12c.

The model is further employed to predict the evolution of the flow stress with strain at 77 K by substituting the corresponding temperature into *Eqs. (6)-(11)*. It is noted that many parameters in the above formula will change as the temperature varies. For example, shear modulus is a temperature-dependent constant and increases with decreasing the temperature. Due to limited reports on CrFeNi MEAs, the temperature dependence of shear modulus is lacking. Here, the shear modulus of the current CrFeNi MEA at 77K is approximately estimated to be 1.1 times than that at 298K, i.e., 76 GPa at 77 K [17]. As described above, φ is a strain-rate and stacking-fault-energy-dependent constants and determined from the initial twin strain and twin fraction. As listed in Section 4.1, the initial twinning strains are 0.7 and 0.2% for Q77 and D77, respectively. Combining ε_{int} and the twin fraction from the microstructure analysis, φ are 0.368 and 0.149 for D77 and Q77, respectively. The fitting results are displayed in Fig. 12d, and the present constitutive model successfully predicts the flow stress behavior for D77. To our knowledge, it is the first constitutive equation to capture the stress-strain curves of HEAs/MEAs under cryogenic temperatures.

Besides, the Johnson-Cook (J-C) model is an empirical viscoplastic-constitutive model, which is widely employed to describe the macroscopic plastic-flow behavior of many different kinds of alloys under high strain rates [62, 111]. Based on the J-C model, the relationships of the strain and stress are fitted, and the fitting results agree well with the experimental results, as presented in Figure S4[39].

5.Conclusion

In the present study, the deformation behaviors of the CrFeNi MEA upon quasi-static and dynamic tension at room (298 K) and cryogenic (77 K) temperatures were investigated. The strain-rate and temperature dependences of deformation behaviors were modeled and discussed. By combining TEM and EBSD techniques, dislocation and twin substructures were carefully investigated to uncover microscopic deformation mechanisms. Based on our observations, the main findings are summarized as follows:

(1) After severe cryo-rolling and annealing at 800℃ for 1 hour, the grain-size distribution of an FCC matrix is heterogeneous due to incomplete recrystallization during low-temperature annealing. Meanwhile, Cr-rich BCC precipitates were formed due to several aspects, including a VEC value of 8, high melting temperature, and large diffusion coefficient of Cr atoms compared with Fe and Ni atoms.

(2) With the temperature decrease from 298 K to 77 K, both the strength and uniform elongation are significantly improved upon quasi-static and dynamic loadings, which is attributed to the activation of twins, causing a dynamic Hall-Petch effect.

(3) Under dynamic loading, a traditional strength-ductility trade-off come into being in the current CrFeNi MEA. The yield strength was significantly increased, since the dislocation motion becomes popular under high strain-rate loading. High-density dislocations together with brittle BCC phases within the FCC matrix cause the reduction of uniform elongations upon dynamic loading.

(4) The strain-rate sensitivity of the CrFeNi MEA (m_s is 0.0371 under quasi-static loading, and m_d is 0.33968 under dynamic loading) is higher than that of pure FCC metals and complex solid-solution alloys, such as stainless steels, HEAs, and MEAs. The strong strain-rate dependence of the yield strength is closely related to the presence of short-range dislocation obstacles, BCC phases, and ultra-fine grains.

(5) A strain rate-dependent and temperature-dependent constitutive model was well established to describe the deformation behaviors of the CrFeNi MEA over a wide range of strain rates from 10^{-4}/s to 4,000/s at room and cryogenic temperatures, the predicted results are in good accord with the experimental data.

Conflicts of interest

The authors declare no competing financial interests.

Acknowledgement

The authors would like to acknowledge the financial support of the Natural Science Foundation of Shanxi Province, China (Nos.201901D111105 and 201901D111114), and the opening project of the State Key Laboratory of Explosion Science and Technology (Beijing Institute of Technology), and the opening project

number is KFJJ20-13M. P. K. L. very much appreciates the supports from (1) the U.S. National Science Foundation [DMR-1611180 and 1809640] with the program directors, Drs. Judith Yang, Gary Shiflet, and Diana Farkas and (2) the Army Office Project [W911NF-13-1-0438 and W911NF-19-2-0049] with the program managers, Drs. Michael P. Bakas, David M. Stepp, and S. Mathaudhu.

Uncategorized References

[1] L. Tang, L. Wang, M. Wang, H. Liu, S. Kabra, Y. Chiu, B. Cai, Synergistic deformation pathways in a TWIP steel at cryogenic temperatures: In situ neutron diffraction, Acta Mater. 200, 943 (2020).
[2] S.S. Sohn, S. Hong, J. Lee, B.C. Suh, S.K. Kim, B.J. Lee, N.J. Kim, S. Lee, Effects of Mn and Al contents on cryogenic-temperature tensile and Charpy impact properties in four austenitic high-Mn steels, Acta Mater. 100, 39 (2015).
[3] T.W. Zhang, S.G. Ma, D. Zhao, Y.C. Wu, Y. Zhang, Z.H. Wang, J.W. Qiao, Simultaneous enhancement of strength and ductility in a NiCoCrFe high-entropy alloy upon dynamic tension: Micromechanism and constitutive modeling, Int. J. Plast. 124, 226 (2020).
[4] B. Gludovatz, A. Hohenwarter, D. Catoor, E.H. Chang, E.P. George, R.O. Ritchie, A fracture-resistant high-entropy alloy for cryogenic applications, Science 345, 1153 (2014).
[5] Y. Tong, D. Chen, B. Han, J. Wang, R. Feng, T. Yang, C. Zhao, Y.L. Zhao, W. Guo, Y. Shimizu, C.T. Liu, P.K. Liaw, K. Inoue, Y. Nagai, A. Hu, J.J. Kai, Outstanding tensile properties of a precipitation-strengthened FeCoNiCrTi0.2 high-entropy alloy at room and cryogenic temperatures, Acta Mater. 165, 228 (2019).
[6] S. Praveen, H.S. Kim, High-Entropy Alloys: Potential Candidates for High-Temperature Applications - An Overview, Adv. Eng. Mater. 20, 1700645 (2018).
[7] W. Li, D. Xie, D. Li, Y. Zhang, Y. Gao, P.K. Liaw, Mechanical behavior of high-entropy alloys, Prog. Mater Sci. 118, 100777 (2021).
[8] E.P. George, W.A. Curtin, C.C. Tasan, High entropy alloys: A focused review of mechanical properties and deformation mechanisms, Acta Mater. 188, 435 (2020).
[9] T. Yang, Y.L. Zhao, J.H. Luan, B. Han, J. Wei, J.J. Kai, C.T. Liu, Nanoparticles-strengthened high-entropy alloys for cryogenic applications showing an exceptional strength-ductility synergy, Scripta Mater. 164, 30 (2019).
[10] Z. Li, S. Zhao, R.O. Ritchie, M.A. Meyers, Mechanical properties of high-entropy alloys with emphasis on face-centered cubic alloys, Prog. Mater Sci. 102, 296 (2019).
[11] Y. Zhang, T.T. Zuo, Z. Tang, M.C. Gao, K.A. Dahmen, P.K. Liaw, Z.P. Lu, Microstructures and properties of high-entropy alloys, Prog. Mater Sci. 61, 1 (2014).
[12] Z. Wu, S.A. David, Z. Feng, H. Bei, Weldability of a high entropy CrMnFeCoNi alloy, Scripta Mater. 124, 81 (2016).
[13] M.A. Hemphill, T. Yuan, G.Y. Wang, J.W. Yeh, C.W. Tsai, A. Chuang, P.K. Liaw, Fatigue behavior of Al0.5CoCrCuFeNi high entropy alloys, Acta Mater. 60, 5723 (2012).
[14] K. Liu, S.S. Nene, M. Frank, S. Sinha, R.S. Mishra, Extremely high fatigue resistance in an ultrafine grained high entropy alloy, Appl. Mater. Today 15, 525 (2019).
[15] E.P. George, D. Raabe, R.O. Ritchie, High-entropy alloys, Nat. Rev. Mater. 4, 515 (2019).
[16] Y. Zhao, D.H. Lee, M.Y. Seok, J.A. Lee, M.P. Phaniraj, J.Y. Suh, H.Y. Ha, J.Y. Kim, U. Ramamurty, J.-i. Jang, Resistance of CoCrFeMnNi high-entropy alloy to gaseous hydrogen embrittlement, Scripta Mater. 135, 54 (2017).
[17] Z. Wu, H. Bei, G.M. Pharr, E.P. George, Temperature dependence of the mechanical properties of equiatomic solid solution alloys with face-centered cubic crystal structures, Acta Mater. 81, 428 (2014).
[18] D.B. Miracle, O.N. Senkov, A critical review of high entropy alloys and related concepts, Acta Mater. 122, 448 (2017).
[19] J. Moon, J.M. Park, J.W. Bae, H.-S. Do, B.-J. Lee, H.S. Kim, A new strategy for designing immiscible

medium-entropy alloys with excellent tensile properties, Acta Mater. 193, 71 (2020).
[20] D.G. Kim, Y.H. Jo, J. Yang, W.M. Choi, H.S. Kim, B.J. Lee, S.S. Sohn, S. Lee, Ultrastrong duplex high-entropy alloy with 2 GPa cryogenic strength enabled by an accelerated martensitic transformation, Scripta Mater. 171, 67 (2019).
[21] N. Kumar, Q. Ying, X. Nie, R.S. Mishra, Z. Tang, P.K. Liaw, R.E. Brennan, K.J. Doherty, K.C. Cho, High strain-rate compressive deformation behavior of the Al0.1CrFeCoNi high entropy alloy, Mater. Des. 86, 598 (2015).
[22] S.G. Ma, Z.M. Jiao, J.W. Qiao, H.J. Yang, Y. Zhang, Z.H. Wang, Strain rate effects on the dynamic mechanical properties of the AlCrCuFeNi2 high-entropy alloy, Mater. Sci. Eng., A 649, 35 (2016).
[23] B. Wang, A. Fu, X. Huang, B. Liu, Y. Liu, Z. Li, X. Zan, Mechanical properties and microstructure of the CoCrFeMnNi high entropy alloy under high strain rate compression, J. Mater. Eng. Perform. 25, 2985 (2016).
[24] T.W. Zhang, Z.M. Jiao, Z.H. Wang, J.W. Qiao, Dynamic deformation behaviors and constitutive relations of an $AlCoCr_{1.5}Fe_{1.5}NiTi_{0.5}$ high-entropy alloy, Scripta Mater. 136, 15 (2017).
[25] J.M. Park, J. Moon, J.W. Bae, M.J. Jang, J. Park, S. Lee, H.S. Kim, Strain rate effects of dynamic compressive deformation on mechanical properties and microstructure of CoCrFeMnNi high-entropy alloy, Mater. Sci. Eng., A 719, 155 (2018).
[26] H. Song, D.G. Kim, D.W. Kim, M.C. Jo, Y.H. Jo, W. Kim, H.S. Kim, B.J. Lee, S. Lee, Effects of strain rate on room- and cryogenic-temperature compressive properties in metastable V10Cr10Fe45Co35 high-entropy alloy, Sci. Rep. 9, 6153 (2019).
[27] Z. Li, S. Zhao, H. Diao, P.K. Liaw, M.A. Meyers, High-velocity deformation of Al0.3CoCrFeNi high-entropy alloy: Remarkable resistance to shear failure, Sci. Rep. 7, 42742 (2017).
[28] C.M. Cao, W. Tong, S.H. Bukhari, J. Xu, Y.X. Hao, P. Gu, H. Hao, L.M. Peng, Dynamic tensile deformation and microstructural evolution of AlxCrMnFeCoNi high-entropy alloys, Mater. Sci. Eng., A 759, 648 (2019).
[29] Z.F. He, N. Jia, H.W. Wang, Y. Liu, D.Y. Li, Y.F. Shen, The effect of strain rate on mechanical properties and microstructure of a metastable FeMnCoCr high entropy alloy, Mater. Sci. Eng., A 776, 138982 (2020).
[30] J. He, Q. Wang, H. Zhang, L. Dai, T. Mukai, Y. Wu, X. Liu, H. Wang, T.G. Nieh, Z. Lu, Dynamic deformation behavior of a face-centered cubic FeCoNiCrMn high-entropy alloy, Sci. Bull. 63, 362 (2018).
[31] H. Kim, J. Park, Y. Ha, W. Kim, S.S. Sohn, H.S. Kim, B.-J. Lee, N.J. Kim, S. Lee, Dynamic tension–compression asymmetry of martensitic transformation in austenitic Fe–(0.4, 1.0)C–18Mn steels for cryogenic applications, Acta Mater. 96, 37 (2015).
[32] K. Wang, X.J. Wang, T.W. Zhang, X. Jin, H.J. Yang, J.W. Qiao, Tuning Cr-rich nanoprecipitation and heterogeneous structure in equiatomic CrFeNi medium-entropy stainless alloys, J. Iron Steel Res. Int., (2021).
[33] W.R. Wang, W.L. Wang, S.C. Wang, Y.C. Tsai, C.H. Lai, J.W. Yeh, Effects of Al addition on the microstructure and mechanical property of AlxCoCrFeNi high-entropy alloys, Intermetallics 26, 44 (2012).
[34] J.C. Rao, H.Y. Diao, V. Ocelík, D. Vainchtein, C. Zhang, C. Kuo, Z. Tang, W. Guo, J.D. Poplawsky, Y. Zhou, P.K. Liaw, J.T.M. De Hosson, Secondary phases in AlxCoCrFeNi high-entropy alloys: An in-situ TEM heating study and thermodynamic appraisal, Acta Mater. 131, 206 (2017).
[35] F. Otto, A. Dlouhý, K.G. Pradeep, M. Kuběnová, D. Raabe, G. Eggeler, E.P. George, Decomposition

of the single-phase high-entropy alloy CrMnFeCoNi after prolonged anneals at intermediate temperatures, Acta Mater. 112, 40 (2016).
[36] Smuk O , Jagodzinski Y., Tarasenko O, S. Smuk, H. Hanninen, Internal friction study of decomposition kinetics of SAF 2507 Type deples strainless steel, Scripta Mater. 40, 321 (1999).
[37] S. Guo, C. Ng, J. Lu, C.T. Liu, Effect of valence electron concentration on stability of fcc or bcc phase in high entropy alloys, J. Appl. Phys. 109, 103505 (2011).
[38] X. Yang, Y. Zhang, Prediction of high-entropy stabilized solid-solution in multi-component alloys, Mater. Chem. Phys. 132, 233 (2012).
[39] See Supplementary materials at XXX for (1) calculation of dislocation density in undeformed samples; (2) calculation of stacking fault energy; (3) thermodynamic evaluations of the Crx(FeNi)100-x alloy systems; (4) SEM fractographs of tensile specimens; (5) XRD patterns of tensile specimens; (6) comparison of experimental and predicted true stress–strain relations from the modified J-C constitutive equations at different strain rates; (7) mechanical properties of current MEAs and some conventional metals/alloys at different strain rates and temperatures; and (8) strain-rate sensitivity of CrFeNi MEAs and other representative FCC metals and alloys.
[40] K.Y. Tsai, M.H. Tsai, J.W. Yeh, Sluggish diffusion in Co–Cr–Fe–Mn–Ni high-entropy alloys, Acta Mater. 61, 4887 (2013).
[41] L.J. Santodonato, Y. Zhang, M. Feygenson, C.M. Parish, M.C. Gao, R.J. Weber, J.C. Neuefeind, Z. Tang, P.K. Liaw, Deviation from high-entropy configurations in the atomic distributions of a multi-principal-element alloy, Nat. Commun. 6, 5964 (2015).
[42] M. Yang, D. Yan, F. Yuan, P. Jiang, E. Ma, X. Wu, Dynamically reinforced heterogeneous grain structure prolongs ductility in a medium-entropy alloy with gigapascal yield strength, Proc. Nati. Acad. Sci. USA 115, 7224 (2018).
[43] Y. Li, Y. Lu, W. Li, M. Khedr, H. Liu, X. Jin, Hierarchical microstructure design of a bimodal grained twinning-induced plasticity steel with excellent cryogenic mechanical properties, Acta Mater. 158, 79 (2018).
[44] Meyers M A , K.K. Chawla, Mechanical Behavior of Materials, Cambridge University Press, Cambridge, 2009.
[45] M. Baig, A.S. Khan, S.-H. Choi, A. Jeong, Shear and multiaxial responses of oxygen free high conductivity (OFHC) copper over wide range of strain-rates and temperatures and constitutive modeling, Int. J. Plast. 40, 65 (2013).
[46] S. Nemat-Nasser, W. Guo, M. Liu, Experimentally-based micromechanical modeling of dynamic response of molybdenum, Scripta Mater. 40, 859 (1999).
[47] Nemat-Nasser, W. Guo, High strain-rate response of commercially pure vanadium, Mech. Mater. 32, 243 (2000).
[48] S. Nemat-Nasser, W. Guo, Flow stress of commercially pure niobium over a broad range of temperatures and strain rates, Mater. Sci. Eng., A 284, 202 (2000).
[49] R. Kapoor, S. Nemat-Nasser, Comparison between high and low strain-rate deformation of tantalum, Matall. Mater. Trans. A 31, 815 (2000).
[50] M. Ardeljan, I.J. Beyerlein, B.A. McWilliams, M. Knezevic, Strain rate and temperature sensitive multi-level crystal plasticity model for large plastic deformation behavior: Application to AZ31 magnesium alloy, Int. J. Plast. 83, 90 (2016).
[51] S. Curtze, V.T. Kuokkala, M. Hokka, P. Peura, Deformation behavior of TRIP and DP steels in tension at different temperatures over a wide range of strain rates, Mater. Sci. Eng., A 507, 124 (2009).

[52] M. Hokka, V.T. Kuokkala, S. Curtze, Dynamic tensile behaviour of TRIP and DP steels at different temperatures, Steel Res. Int. 80, 137 (2009).
[53] W.G. Guo, S. Nemat Nasser, Flow stress of Nitronic-50 stainless steel over a wide range of strain rates and temperatures, Mech. Mater. 38, 1090 (2006).
[54] F. Abed, G. Voyiadjis, Plastic deformation modeling of AL-6XN stainless steel at low and high strain rates and temperatures using a combination of bcc and fcc mechanisms of metals, Int. J. Plast. 21, 1618 (2005).
[55] J. Zhang, Y. Wang, Effect of strain rate on the tension behavior of Ti–6.6Al–3.3Mo–1.8Zr–0.29Si alloy at low temperatures, Mater. Sci. Eng., A 605, 59 (2014).
[56] R.U. Vaidya, Z. Jin, C. Cady, G.T.G. Iii, D.P. Butt, A comparative study of the strain rate and temperature dependent compression behavior of Ti-46.5Al-3Nb-2Cr-0.2W and Ti-25Al-10Nb-3V-1Mo intermetallic alloys, Scripta Mater. 41, 569 (1999).
[57] J. Wang, W.-G. Guo, X. Gao, J. Su, The third-type of strain aging and the constitutive modeling of a Q235B steel over a wide range of temperatures and strain rates, Int. J. Plast. 65, 85 (2015).
[58] J. Ding, Q. Yu, M. Asta, R.O. Ritchie, Tunable stacking fault energies by tailoring local chemical order in CrCoNi medium-entropy alloys, Proc, Nat. Acad. Sci. USA 115, 8919 (2018).
[59] G. Bonny, N. Castin, D. Terentyev, Interatomic potential for studying ageing under irradiation in stainless steels: the FeNiCr model alloy, Modell. Simul. Mater. Sci. Eng. 21, 5897 (2013).
[60] H. Kim, M. Kang, H.J. Jung, H.S. Kim, S. Lee, Mechanisms of toughness improvement in Charpy impact and fracture toughness tests of non-heat-treating cold-drawn steel bar, Mater. Sci. Eng., A 571, 38 (2013).
[61] W.S. Lee, C.F. Lin, Impact properties and microstructure evolution of 304L stainless steel, Mater. Sci. Eng., A 308, 124 (2001).
[62] L. Wang, J.W. Qiao, S.G. Ma, Z.M. Jiao, T.W. Zhang, G. Chen, D. Zhao, Y. Zhang, Z.H. Wang, Mechanical response and deformation behavior of Al 0.6 CoCrFeNi high-entropy alloys upon dynamic loading, Mater. Sci. Eng., A 727, 208 (2018).
[63] Z. Wang, W. Lu, H. Zhao, C.H. Liebscher, Z. Li, Ultrastrong lightweight compositionally complex steels via dual-nanoprecipitation, Sci. Adv. 6, 9543 (2020).
[64] M. Bönisch, Y. Wu, H. Sehitoglu, Twinning-induced strain hardening in dual-phase FeCoCrNiAl0.5 at room and cryogenic temperature, Sci. Rep. 8, 10663 (2018).
[65] R.P. Reed, The spontaneous martensitic transformations in 18% Cr, 8% Ni steels, Acta Metall. 10, 865 (1962).
[66] D. Wei, X. Li, S. Schönecker, J. Jiang, W.M. Choi, B.J. Lee, H.S. Kim, A. Chiba, H. Kato, Development of strong and ductile metastable face-centered cubic single-phase high-entropy alloys, Acta Mater. 181, 318 (2019).
[67] S. Zhao, Z. Li, C. Zhu, Wen Yang, Zhouran Zhang, David E. J. Armstrong, Patrick S. Grant, Robert O. Ritchie, M.A. Meyers, Amorphization in extreme deformation of the CrMnFeCoNi high-entropy alloy, Sci. Adv. 7, 3108 (2021).
[68] K. Ming, W. Lu, Z. Li, X. Bi, J. Wang, Amorphous bands induced by low temperature tension in a non-equiatomic CrMnFeCoNi alloy, Acta Mater. 188, 354 (2020).
[69] G. Laplanche, A. Kostka, C. Reinhart, J. Hunfeld, G. Eggeler, E.P. George, Reasons for the superior mechanical properties of medium-entropy CrCoNi compared to high-entropy CrMnFeCoNi, Acta Mater. 128, 292 (2017).
[70] J. Lu, L. Hultman, E. Holmström, K.H. Antonsson, M. Grehk, W. Li, L. Vitos, A. Golpayegani,

Stacking fault energies in austenitic stainless steels, Acta Mater. 111, 39 (2016).
[71] Y. Wang, B. Liu, K. Yan, M. Wang, S. Kabra, Y.-L. Chiu, D. Dye, P.D. Lee, Y. Liu, B. Cai, Probing deformation mechanisms of a FeCoCrNi high-entropy alloy at 293 and 77 K using in situ neutron diffraction, Acta Mater. 154, 79 (2018).
[72] G.B. Olson, M. Cohen, Kinetics of strain-induced martensitic nucleation, Matall. Mater. Trans. A 6, 791 (1975).
[73] S. Curtze, V.T. Kuokkala, A. Oikari, J. Talonen, H. Hänninen, Thermodynamic modeling of the stacking fault energy of austenitic steels, Acta Mater. 59, 1068 (2011).
[74] S. Allain, J.P. Chateau, O. Bouaziz, S. Migot, N. Guelton, Correlations between the calculated stacking fault energy and the plasticity mechanisms in Fe–Mn–C alloys, Mater. Sci. Eng., A 387-389, 158 (2004).
[75] Yakubtsov I A, Ariapour A , D.D. Perovic, Effect of nitrogen on stacking fautl energy of f.c.c iron-based alloys, Acta Mater. 47, 1271 (1999).
[76] C.G. Rhodes, A.W. Thompson, The composition dependence of stacking fault energy in austenitic stainless steels, Matall. Mater. Trans. A 8, 1901 (1977).
[77] K. Ishieda, Direct estimation of stacking fault energy by thermodynamic analysis, Phys. Status Solidi A 36, 717 (1976).
[78] B.J. Lee, A Thermodynamic Evaluation of the Cr-Mn and Fe-Cr-Mn Systems, Matall. Mater. Trans. A 24A, 1919 (1993).
[79] L. Meng, P. Yang, Q. Xie, H. Ding, Z. Tang, Dependence of deformation twinning on grain orientation in compressed high manganese steels, Scripta Mater. 56, 931 (2007).
[80] Meyers M A, Vohringer O , V.A. Lubarda, The onset of twinning in metals: a constitutive description, Acta Mater. 49, 4025 (2001).
[81] Christian J W , S. Mahajant, Deformation twinning, Prog. Mater Sci. 39, 1 (1995).
[82] S. Curtze, V.T. Kuokkala, Dependence of tensile deformation behavior of TWIP steels on stacking fault energy, temperature and strain rate, Acta Mater. 58, 5129 (2010).
[83] Y.H. Jo, S. Jung, W.M. Choi, S.S. Sohn, H.S. Kim, B.J. Lee, N.J. Kim, S. Lee, Cryogenic strength improvement by utilizing room-temperature deformation twinning in a partially recrystallized VCrMnFeCoNi high-entropy alloy, Nat. Commun. 8, 15719 (2017).
[84] G. Laplanche, A. Kostka, O.M. Horst, G. Eggeler, E.P. George, Microstructure evolution and critical stress for twinning in the CrMnFeCoNi high-entropy alloy, Acta Mater. 118, 152 (2016).
[85] D.R. Steinmetz, T. Jäpel, B. Wietbrock, P. Eisenlohr, I. Gutierrez-Urrutia, A. Saeed–Akbari, T. Hickel, F. Roters, D. Raabe, Revealing the strain-hardening behavior of twinning-induced plasticity steels: Theory, simulations, experiments, Acta Mater. 61, 494 (2013).
[86] T.S. Byun, On the stress dependence of partial dislocation separation and deformation microstructure in austenitic stainless steels, Acta Mater. 51, 3063 (2003).
[87] W. Woo, J.S. Jeong, D.K. Kim, C.M. Lee, S.H. Choi, J.Y. Suh, S.Y. Lee, S. Harjo, T. Kawasaki, Stacking Fault Energy Analyses of Additively Manufactured Stainless Steel 316L and CrCoNi Medium Entropy Alloy Using In Situ Neutron Diffraction, Sci. Rep. 10, 1350 (2020).
[88] I. Gutierrez-Urrutia, D. Raabe, Dislocation and twin substructure evolution during strain hardening of an Fe–22wt.% Mn–0.6wt.% C TWIP steel observed by electron channeling contrast imaging, Acta Mater. 59, 6449 (2011).
[89] P. Larour, P. Verleysen, K. Dahmen, W. Bleck, Strain Rate Sensitivity of Pre-Strained AISI 301LN2B Metastable Austenitic Stainless Steel, Steel Res. Int. 84, 72 (2013).

[90] Y.H. Jo, D.G. Kim, M.C. Jo, K.Y. Doh, S.S. Sohn, D. Lee, H.S. Kim, B.J. Lee, S. Lee, Effects of deformation–induced BCC martensitic transformation and twinning on impact toughness and dynamic tensile response in metastable VCrFeCoNi high–entropy alloy, J. Alloys Compd. 785, 1056 (2019).
[91] R. Bobbili, V. Madhu, A modified Johnson-Cook model for FeCoNiCr high entropy alloy over a wide range of strain rates, Mater. Lett. 218, 103 (2018).
[92] R.W. Armstrong, S.M. Walley, High strain rate properties of metals and alloys, Int. Mater. Rev. 53, 105 (2008).
[93] Y.L. S. Netat-Nasser, Flow stress of f.c.c. polycrystals with application to OFHC Cu, Acta Mater. 46, 565 (1998).
[94] A.S. Khan, R. Liang, Behaviors of three BCC metal over a wide range of strain rates and temperatures: experiments and modeling, Int. J. Plast. 15, 1089 (1999).
[95] Joshua A. Lichtenfeld, Martin C. Mataya, C.J.V. Tyne, Effect of strain rate on stress-strain behavior of alloy 309 and 304L austenitic stainless steel, Matall. Mater. Trans. A 37A, 147 (2006).
[96] W.S. Lee, C.F. Lin, T.J. Liu, Strain rate dependence of impact properties of sintered 316L stainless steel, J. Nucl. Mater. 359, 247 (2006).
[97] L.K. O. Grassel, G. Frommeyer , L.W. Meyer, High strength Fe±Mn±(Al, Si) TRIP/TWIP steels development-properties-application, Int. J. Plast. 16, 1391 (2000).
[98] G. Dirras, H. Couque, L. Lilensten, A. Heczel, D. Tingaud, J.P. Couzinié, L. Perrière, J. Gubicza, I. Guillot, Mechanical behavior and microstructure of Ti20Hf20Zr20Ta20Nb20 high-entropy alloy loaded under quasi-static and dynamic compression conditions, Mater. Charact. 111, 106 (2016).
[99] Y.F. Xue, H.N. Cai, L. Wang, F.C. Wang, H.F. Zhang, Effect of loading rate on failure in Zr-based bulk metallic glass, Mater. Sci. Eng., A 473, 105 (2008).
[100] M.C. Li, M.Q. Jiang, S. Yang, F. Jiang, L. He, J. Sun, Effect of strain rate on yielding strength of a Zr-based bulk metallic glass, Mater. Sci. Eng., A 680, 21 (2017).
[101] R.S. Mishra, N. Kumar, M. Komarasamy, Lattice strain framework for plastic deformation in complex concentrated alloys including high entropy alloys, Mater. Sci. Technol. 31, 1259 (2015).
[102] C. Lee, G. Song, M.C. Gao, R. Feng, P. Chen, J. Brechtl, Y. Chen, K. An, W. Guo, J.D. Poplawsky, S. Li, A.T. Samaei, W. Chen, A. Hu, H. Choo, P.K. Liaw, Lattice distortion in a strong and ductile refractory high-entropy alloy, Acta Mater. 160, 158 (2018).
[103] C. Lee, Y. Chou, G. Kim, M.C. Gao, K. An, J. Brechtl, C. Zhang, W. Chen, J.D. Poplawsky, G. Song, Y. Ren, Y.-C. Chou, P.K. Liaw, Lattice-Distortion-Enhanced Yield Strength in a Refractory High-Entropy Alloy, Adv. Mater. 32, 2004029 (2020).
[104] B. Yin, S. Yoshida, N. Tsuji, W.A. Curtin, Yield strength and misfit volumes of NiCoCr and implications for short-range-order, Nat. Commun. 11, 2507 (2020).
[105] Q. Ding, Y. Zhang, X. Chen, X. Fu, D. Chen, S. Chen, L. Gu, F. Wei, H. Bei, Y. Gao, M. Wen, J. Li, Z. Zhang, T. Zhu, R.O. Ritchie, Q. Yu, Tuning element distribution, structure and properties by composition in high-entropy alloys, Nature 574, 223 (2019).
[106] M. Komarasamy, N. Kumar, R.S. Mishra, P.K. Liaw, Anomalies in the deformation mechanism and kinetics of coarse-grained high entropy alloy, Mater. Sci. Eng., A 654, 256 (2016).
[107] Q. Zhang, J. Zhang, Y. Wang, Effect of strain rate on the tension–compression asymmetric responses of Ti–6.6Al–3.3Mo–1.8Zr–0.29Si, Mater. Des. 61, 281 (2014).
[108] J. Tao, B. Gu, L. Chen, J. Zhou, Tension–Compression Asymmetry of Commercially Pure Titanium: Strain Rate Sensitivity and Microstructure Evolution, JOM 71, 2280 (2019).
[109] W.D. Liu, K.X. Liu, Notable internal thermal effect on the yielding of metallic glasses, Appl. Phys.

Lett. 100, 141904 (2012).
[110] J.L. Dong, T.W. Zhang, Z. Wang, X.H. Shi, J.W. Qiao, Z.H. Wang, Y.C. Wu, Homogeneous elongation and distinguishing work hardening in La-based metallic glass composites upon dynamic tension, Mater. Sci. Eng., A 736, 329 (2018).
[111] M.A. Meyers, Dynamic behavior of materials, John Wiley and Sons, New York, 1994.
[112] Zerilli F. J. , R.W. Armstrong, The effect of dislocation drag on the stress-strain behavior of f.c.c metals, Acta Metall. 40, 1803 (1992).
[113] F.J. Zerilli, R.W. Armstrong, Dislocation‐mechanics‐based constitutive relations for material dynamics calculations, J. Appl. Phys. 61, 1816 (1987).
[114] C. Zener, J.H. Hollomon, Effect of Strain Rate Upon Plastic Flow of Steel, J. Appl. Phys. 15, 22 (1944).
[115] J.I. Lee, H.S. Oh, E.S. Park, Manipulation of σy/κ ratio in single phase FCC solid-solutions, Appl. Phys. Lett. 109, 061906 (2016).
[116] T.H. Courtney, Mechanical Behavior of Materials, McGraw-Hill Press, Waveland, 2004.
[117] S.W. Wu, G. Wang, Q. Wang, Y.D. Jia, J. Yi, Q.J. Zhai, J.B. Liu, B.A. Sun, H.J. Chu, J. Shen, P.K. Liaw, C.T. Liu, T.Y. Zhang, Enhancement of strength-ductility trade-off in a high-entropy alloy through a heterogeneous structure, Acta Mater. 165, 444 (2019).
[118] Y. Estrin, Dislocation-Density-Related Constitutive Modeling, Academic Pressed, San Diego, 1996.
[119] U.F. Kocks, H. Mecking, Physics and phenomenology of strain hardening: the FCC case, Prog. Mater Sci. 48, 171 (2003).
[120] Z.Y. Liang, X. Wang, W. Huang, M.X. Huang, Strain rate sensitivity and evolution of dislocations and twins in a twinning-induced plasticity steel, Acta Mater. 88, 170 (2015).
[121] R.L. Fullman, Measurement of Particle Sizes in Opaque Bodies, JOM 5, 447 (1953).

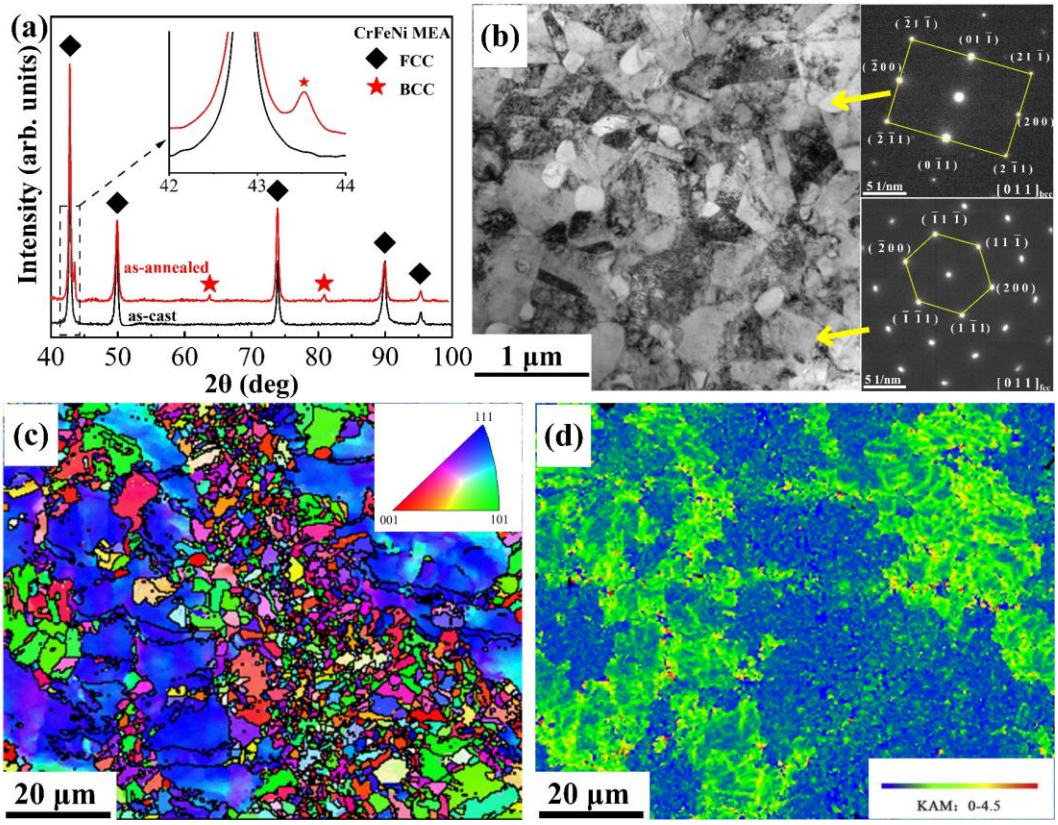

Figure 1. Microstructures of CrFeNi MEAs. (a) XRD patterns of as-cast and as-annealed samples, showing BCC phases, (b) Bright-field TEM micrographs with the corresponding SAED patterns of as-annealed CrFeNi MEAs, (c) EBSD IPF maps of an-annealed CrFeNi MEAs, showing a heterogeneous structure, and (d) corresponding KAM maps to (c).

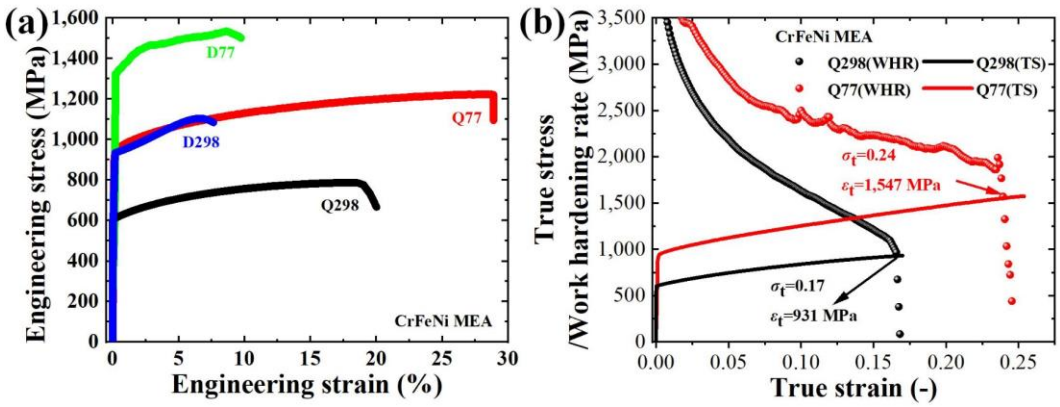

Figure 2. (a) Quasi-static and dynamic engineering stress-strain curves tested at room and cryogenic temperatures of the CrFeNi MEAs. The alloys both exhibit ductile dimpled structures, and (b) true stress-true strain curves and work-hardening rate versus true strain curves of Q298 and Q77.

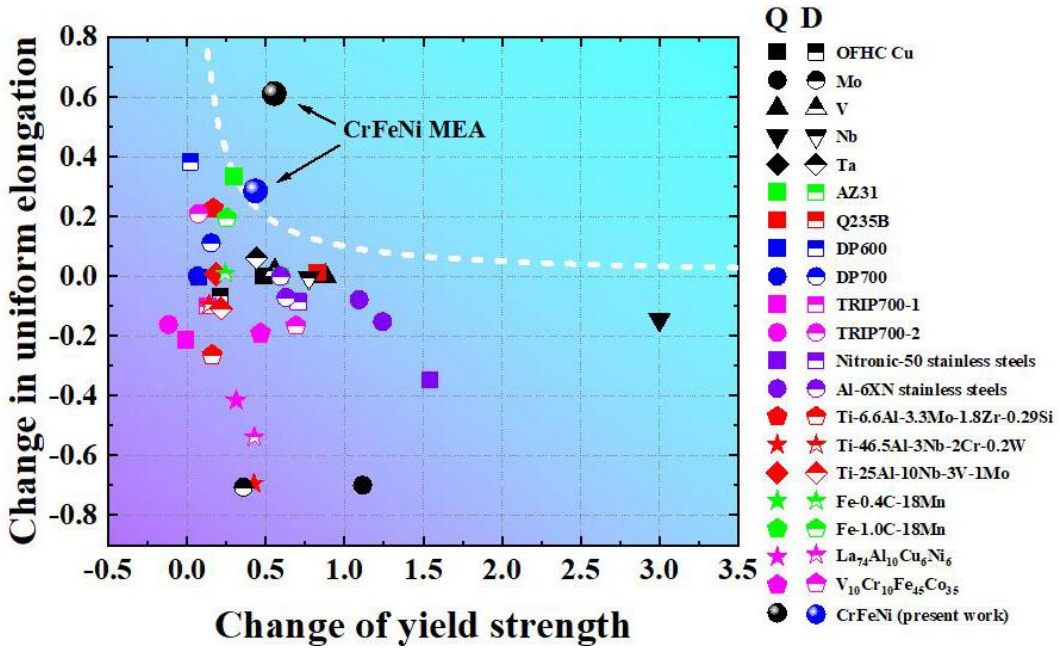

Figure 3 Plots of change of UE and change of YS of some conventional metals and alloys, HEAs, and metallic glasses matrix composites. ($V_C = \frac{V_{77}-V_{298}}{V_{77}}$).

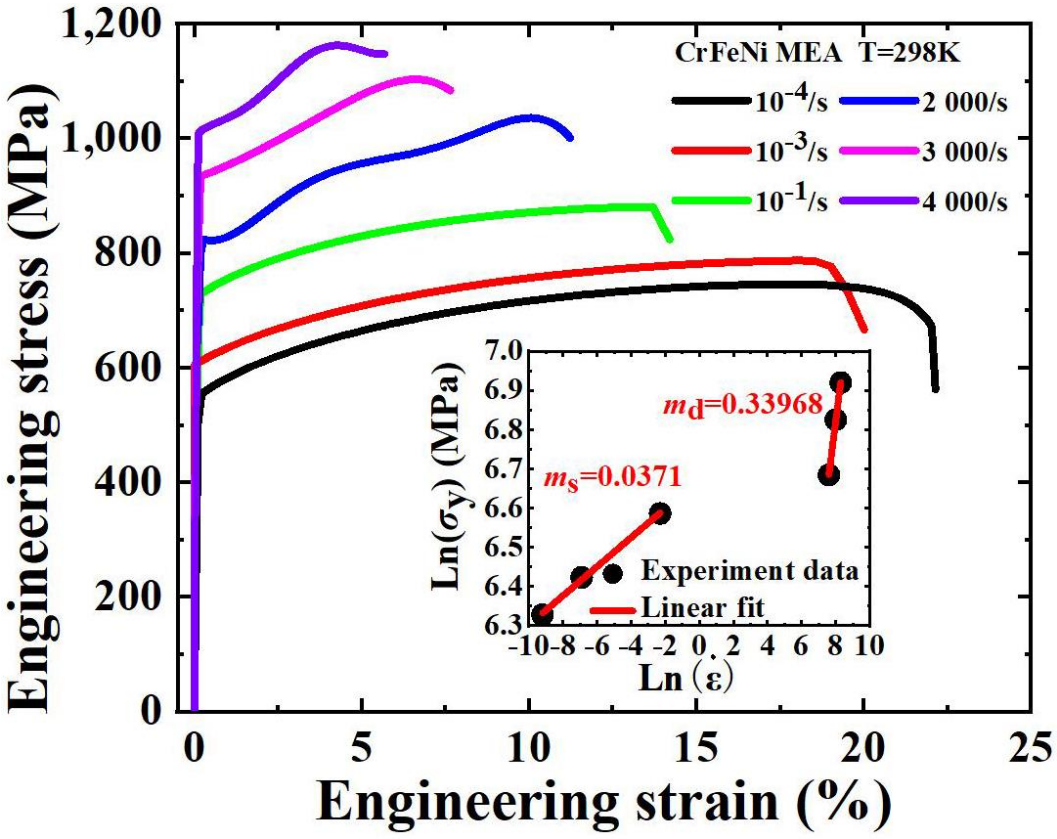

Figure 4 Engineering stress-strain curves of current CrFeNi MEAs at different strain rates. The inset shows the variation of yielding strengths with strain rates at two distinct regions for CrFeNi MEAs.

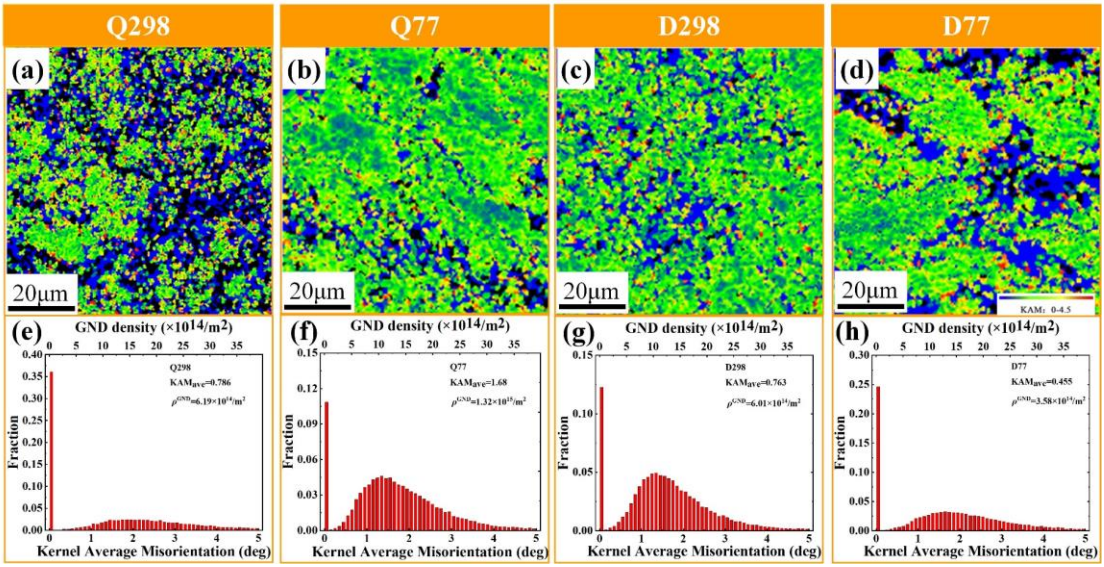

Figure 5. Dislocations with grains after fracture. (a), (b), (c), and (d) are EBSD KAM maps of Q298, Q77, D298, and D77, respectively. (e)-(h) the statistical histograms of the KAM/GND density evolution of Q298, Q77, D298, and Q77, respectively. The average values are shown in the figure.

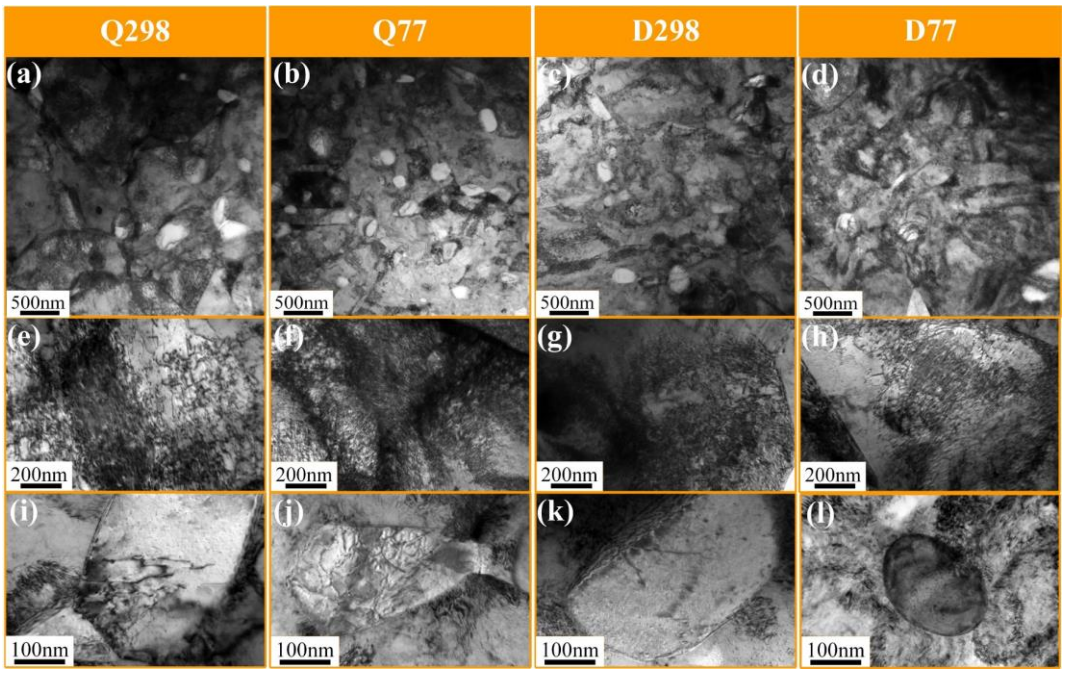

Figure 6. Dislocation structures of the alloys after fracture. (a)-(d) bright-field TEM images of Q298, Q77, D298, and Q77, respectively, (e-h) Dislocations in the FCC matrix of Q298, Q77, D298, and Q77, respectively, and (i-l) Dislocations in the Cr-rich BCC precipitates of Q298, Q77, D298, and Q77, respectively.

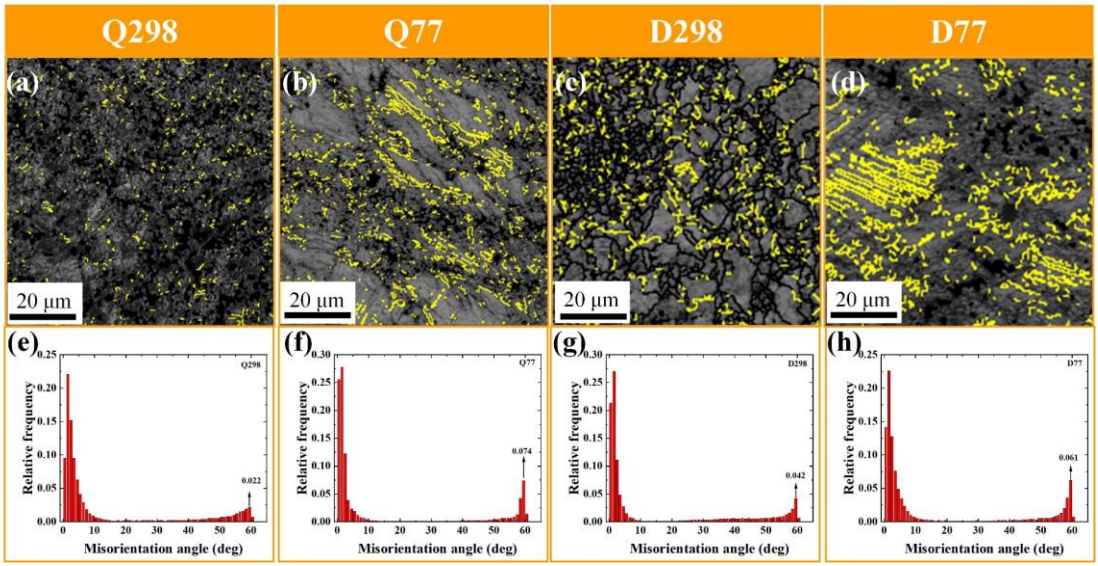

Figure 7. Twins of the alloys after fracture. (a), (b), (c), and (d) are EBSD band-contrast maps with Σ3 twin boundaries of Q298, Q77, D298, and Q77, respectively, and (e)-(h) the statistical histogram of misorientation angle of Q298, Q77, D298, and Q77, respectively.

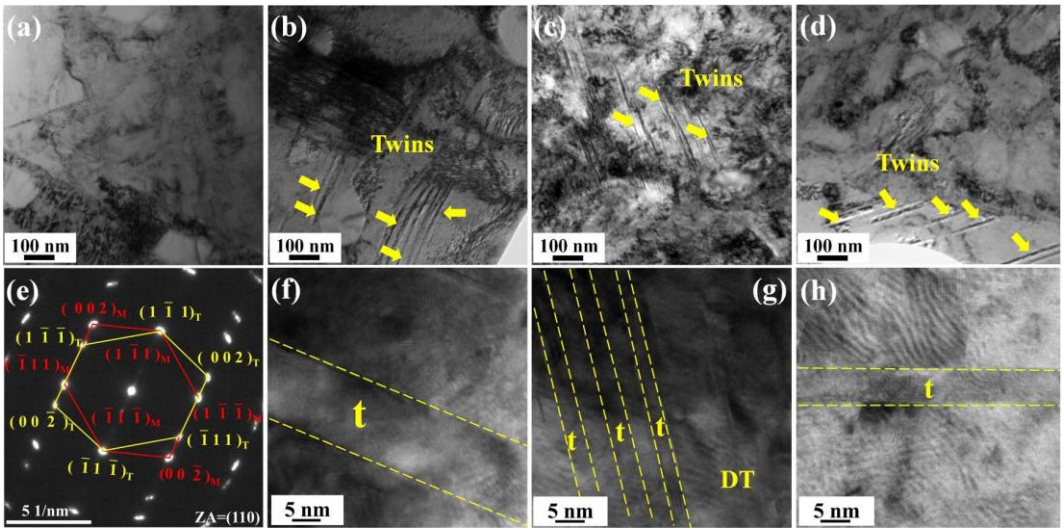

Figure 8. Twins of the alloys after fracture. (a)-(d) bright-field TEM images of Q298, Q77, D298, and Q77, respectively, (e) selected area electron diffraction (SAED) map of parallel bands in (b). The SAED maps of parallel bands in (c) and (d) are similar, and (f-h) twins in the FCC matrices of Q77, D298, and Q77, respectively.

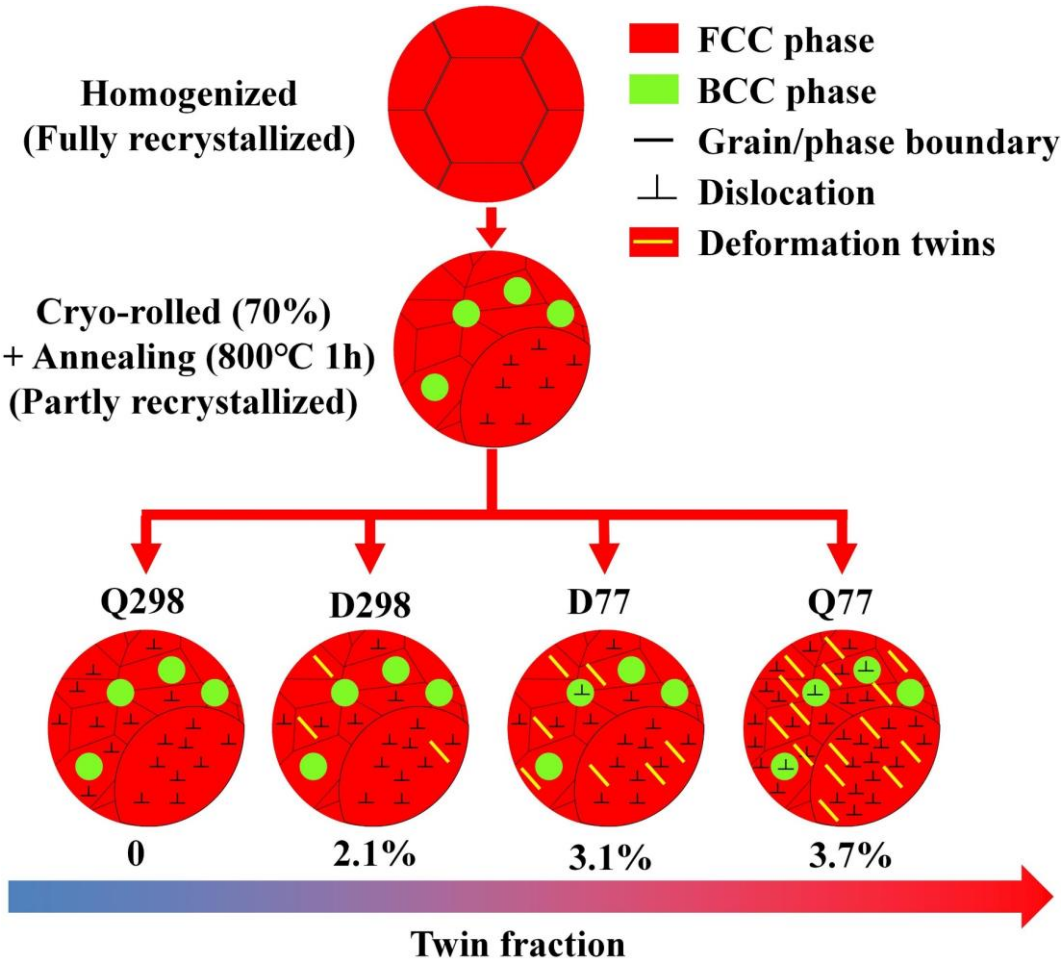

Figure 9. Schematic diagrams of microstructural evolution under different conditions.

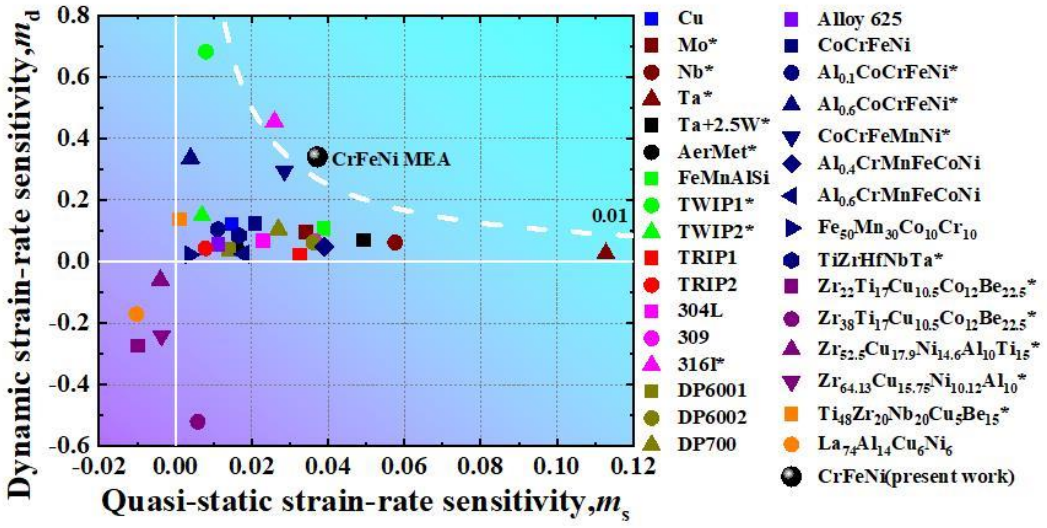

Figure 10. Plots of quasi-static SRS (m_s) and dynamic SRS (m_d) of some conventional alloys, HEAs, MEAs, and metallic glasses. (*: data from compression experiments)

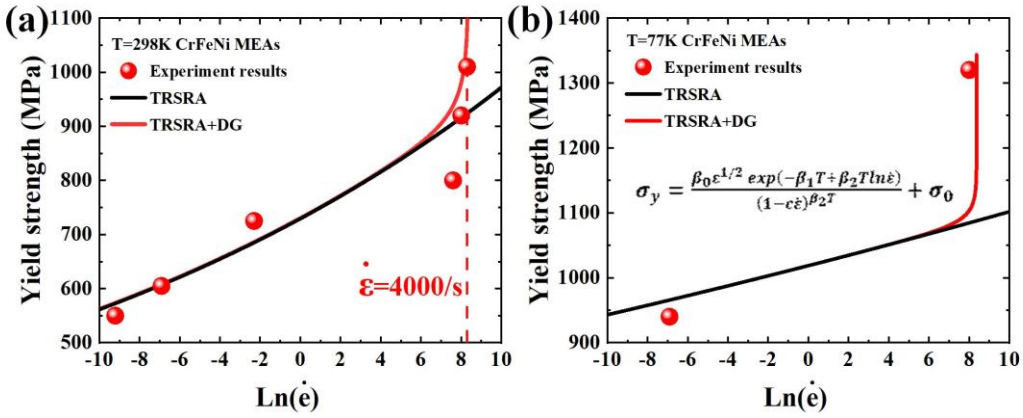

Figure 11. (a) Modeling the strain-rate dependence of the YS at 298K. The black and red threads are thermal activation equation predictions without and with dislocation drag, respectively, and (b) the comparison of experimental and predicted yield strengths at 77K with dislocation drag.

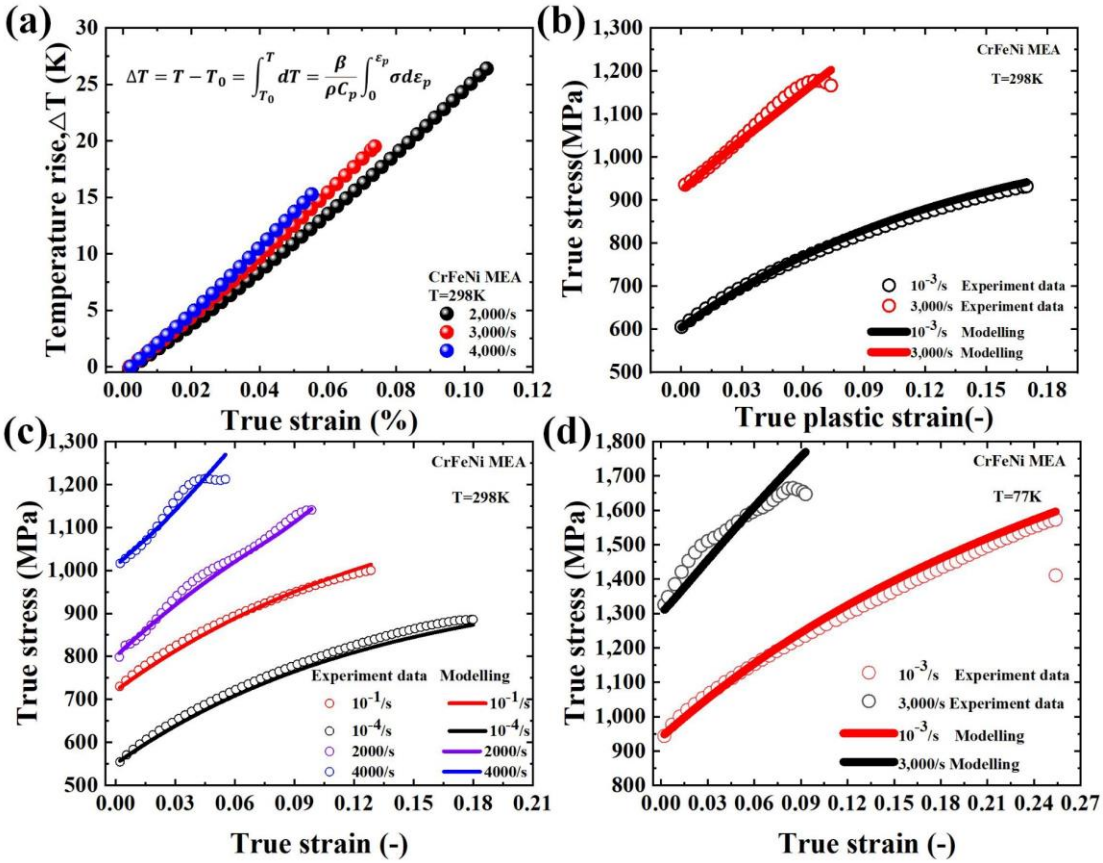

Figure 12. (a) Adiabatic temperature rising of current CrFeNi MEAs under dynamic loading, and (b) experimental true stress after yielding of CrFeNi MEA and corresponding curves from best fitting. Experimental true stress after yielding and corresponding predicted results at 298K (c) and 77K (d).

Table 1 Chemical compositions of phases for CrFeNi MEAs

Phase	Average size	Volume fraction	Chemical composition/at. %		
			Cr	Fe	Ni
FCC	760 nm	~ 90%	34.11	33.83	32.06
BCC	355 nm	~ 10%	86.49	11.58	1.93

Table 2 Comparison of yield strengths, ultimate strengths, and uniform elongations of the CrFeNi MEAs under different conditions.

T(K)	$\dot{\varepsilon}$(/s)	σ_y(MPa)	ε_{uni}(%)	σ_{uti}(MPa)	$\sigma_{uti} - \sigma_y$(MPa)
77K	10^{-3}	940 ± 7	29 ± 2	1,220 ± 10	280
	3,000	1,320±12	9 ± 1	1,530 ± 15	210
298K	10^{4}	550 ± 8	21 ± 1	745 ± 6	195
	10^{-3}	605 ± 6	18 ± 1	785 ± 12	180
	10^{-1}	725 ± 9	14 ± 2	845 ± 10	120
	2,000	800 ± 13	10 ± 1	1,010 ± 18	210
	3,000	920 ± 15	7 ± 1	1,110 ± 15	190
	4,000	1,010 ± 10	4 ± 1	1,160 ± 22	150

(σ_y: strain rate, σ_y: yield strength, ε_{uni}: uniform elongation, σ_{uti}: ultimate tensile stress, $\sigma_{uti} - \sigma_y$: the difference between the yield strength and ultimate tensile stress)

Table 3 Materials' constants and parameters in the constitutive model.

	Description	Value
M	Taylor factor	3.06
G	Shear modulus	69 GPa (298K)
		76 GPa (77K)
ρ_{int}	Initial dislocation density	2.254×10^{13} m^{-2}
α	Dislocation interaction strength	0.4
b	Burgers vector for perfect dislocation	0.254 nm
i_{Δ}	Scaling constant for twin spacing	0.14
C_{v}	Heat capacity	0.446 J/g K
β	Plastic energy-heat conversion fraction	0.9
T_{m}	Melting temperature	1,875 K
ρ	Mass density	7.98 g/cm^3
γ_{SF}	Stacking fault energy	65.85 mJ/m^2（298K）
		43.30 mJ/m^2 (77K)
		2.5 nm (D298)
t	Average twin thickness	11.6 nm (Q77)
		5.3 nm (D77)
		0.653 (D298)
φ	Material constant	0.149 (Q77)
		0.368 (D77)
K	Boltzmann constant	1.380649×10^{23}
A	Material parameter	2.43×10^{19} J 298K
		2.78×10^{19} J 77K
$\dot{\varepsilon}_0$	Reference strain rate	10^7/s
k_0	Athermal recovery factor	3.21
k_1	Dislocation hardening factor (S)	3.06×10^{-2}
k_2	Dislocation hardening factor (D)	3.59×10^{-2}